ORIGINAL ARTICLE



The influence of obstacle geometric fidelity on blast wave propagation: a reduced-scale case study examining the role of the grain siloes in the 2020 Beirut explosion

J. W. Denny¹ · D. G. Farrimond^{2,3} · S. Gabriel⁴ · S. K. C. Yuen⁴ · S. Rigby^{2,5} · S. Al-Hajj⁶ · S. Langdon²

Received: 26 March 2025 / Revised: 10 June 2025 / Accepted: 18 June 2025 © The Author(s) 2025

Abstract

In the field of blast protection engineering, it remains challenging to validate large, complex numerical models and the implications of modelling assumptions relating to how structures are represented (e.g., geometric fidelity) are not well understood. This paper presents experimental work addressing these two issues, in the context of the 2020 Beirut explosion, which remains an important case study for understanding urban blast effects. A series of reduced-scale (1:250) blast tests examined shielding effects caused by the Beirut grain siloes and investigated the influence of the siloes' geometric fidelity on blast loading. Rigid obstacles were constructed at two geometric fidelities: "rectangular" (i.e., cuboid) and "accurate", with closer resemblance to the siloes. Pressure gauges were mounted at multiple locations but at fixed blast scaled distances to examine blast-obstacle interaction behaviour. Additionally, Viper::Blast was used to perform computational fluid dynamics analyses of the tests. Experimental findings confirmed significant shielding (reduced pressure and specific impulse) locally behind the siloes ($Z < 3 \text{ m/kg}^{1/3}$), although models indicated that these effects ceased further afield ($Z > 5 \text{ m/kg}^{1/3}$). Overall, blast wave parameters did not exhibit significant differences between the rectangular and accurate representation of the siloes geometry, except for minor differences (10%) in peak overpressures in localised zones. Numerical models confirmed that these discrepancies were caused by differing blast wave scattering, diffraction, and superposition behaviour attributed to the siloes outer geometry. The results suggest that city-scale blast loading analyses can yield reliable results through idealising structures as simplified cuboidal obstacles. These findings will be of direct relevance to blast protection practitioners and researchers concerned with modelling urban blast scenarios.

 $\textbf{Keywords} \ \ Blast-obstacle \ interaction \cdot Geometry \ effects \cdot Beirut \ grain \ siloes \cdot Blast \ propagation \cdot The \ Beirut \ blast$

Communicated by C. E. Needham.

Published online: 02 September 2025

☑ J. W. Denny Jack.Denny@soton.ac.uk

- Department of Civil Engineering, Faculty of Engineering and Physical Sciences, University of Southampton, Southampton, IJK
- School of Mechanical, Aerospace & Civil Engineering, University of Sheffield, Mappin Street, Sheffield S1 3JD, UK
- Blastech Ltd., The Innovation Centre, 217 Portobello, Sheffield S1 4DP, UK
- Blast Impact and Survivability Research Unit (BISRU), Department of Mechanical Engineering, University of Cape Town, Cape Town, South Africa

1 Introduction

Numerical modelling capabilities have far outpaced those of practical studies in the field of blast protection engineering. To this extent, there is currently a substantial disparity between the scale and fidelity with which numerical models can be solved, compared to the relatively coarse-grained, spatially simple arrangements used in experimental work. This presents a substantial and dual-aspect challenge to the research community, namely: (a) high fidelity, large, geo-

- Arup Resilience, Security & Risk, 3 Piccadilly Place, Manchester M1 3BN, UK
- Department of Epidemiology and Population Health, Faculty of Health Sciences, American University of Beirut, Beirut, Lebanon



metrically complex numerical models cannot be rigorously validated, and (b) the implications of certain (necessary) modelling choices with regard to how structures are represented (e.g., degree of rigidity and geometric fidelity) are not well understood.

This paper presents experimental work aimed at addressing these two problems, in the context of the 2020 Beirut explosion, which remains an important case study in order to gain a deeper understanding of blast effects in urban areas, particularly given the increasingly urbanised nature of explosive violence. On 4 August 2020, approximately 2750 tonnes of ammonium nitrate (AN) stored in the port of Beirut detonated, causing a catastrophic explosion with an equivalent yield of approximately 500 t TNT [1]; the largest non-nuclear explosion to have occurred in a built-up populated area [2, 3]. The explosion caused at least 218 fatalities, injured more than 7000, and left an estimated 300,000 people homeless [4]. Large parts of the city were damaged including 80% of the city's hospitals [5], with physical damages costs estimated at US\$4.6 billion [6].

Despite their close proximity to the epicentre, a majority of the Beirut grain siloes structure remained standing following the explosion, making them a site of significant interest (Fig. 1). The Beirut grain siloes were located in the port of Beirut directly adjacent to the "Hangar 12" warehouse, which contained the AN that detonated (Fig. 1).

Following the disaster, multiple studies have used numerical approaches and fieldwork to investigate the Beirut grain siloes structural response to the blast [3] and structural health monitoring of the siloes [4]. Given that a substantial proportion of the siloes remained standing following the blast (Fig. 1b), there was speculation that the Beirut grain siloes had lessened the severity of the blast wave [5–7] and shielded the blast wave away from the Beirut Central District (Fig. 2), located to the west of the explosion.

However, others have suggested that the siloes did not have a significant role in shielding nearby structures from substantial damage. Using numerical modelling results and satellite images of structures immediately behind the siloes before and after the blast, Temsah et al. [3] argue that the siloes did not have a significant protective role as they were destroyed.

Fig. 1 The Beirut grain siloes before (left, [1]) and after (right, 5 August 2020, [2], courtesy of Nabil Ismail) the port explosion, showing most of the monolithic structure remaining





A numerical study by Zehil [8] suggested that the reduced structural damage severity observed in western Beirut was attributed to having a greater distance from the explosion rather than the siloes' protective influence. Zehil [8] suggested that shielding from the siloes was relatively localised, diminishing by a distance of 450 m from the explosion. The study simplifies the geometry and arrangement of the siloes structure (cuboid obstacle with half-symmetry), so the influence of the siloes' unique, undulating surface geometry on the blast wave propagation (and local shielding effects) remains unknown.

The simplification of obstacle geometry is a common approach in existing research into blast effects in urban settings, largely due to (memory and run time) constraints on model fidelity. In prior experimental studies exploring blast wave propagation and shielding effects, rigid obstacles with relatively simple geometry (i.e., cuboid structures with smooth surfaces) are typically specified to represent individual buildings [9, 10]. Replicating urban blast events experimentally proves difficult at full scale, which has resulted in numerous studies being conducted through equivalent means such as compressed gas bubbles [11, 12] or exploding wires [13]; however, these do not foster the same underlying detonation process as a real explosive event would. Farrimond et al. [14] presented successful experimental results of utilising Hopkinson–Cranz [15, 16] scaling laws for gramm-scale high explosive detonations when compared to larger freeair empirical predictions. Gabriel et al. [17] undertook both experimental and numerical studies of laboratory-scale blast events interacting with scaled obstacles and compared these results to a full-scale trial [10]. Morsel et al. [9] conducted similar laboratory-scale events using exploding wire systems to investigate shock-load-induced material response of structures, scaled through varying material properties. These results suggest that the relevant shock physics is generally captured and understood in simple scenarios, but when the geometry of the domain becomes more complex, characterisation becomes more challenging and the behaviour less understood.

Similarly, in numerical studies, models have explored shielding of individual structures [18–20] and different urban



Fig. 2 Satellite image of the Beirut port and the neighbouring areas of the city of Beirut, on 5 August 2020 (i.e., the day after the large-scale explosion) [8]. Image ©2024 CNES/Airbus and Google Earth



layouts/street geometries [21–24], although typically using simplified geometries. For example, Valsamos et al. [24] performed numerical models of the Beirut Blast using Open Street Map (OSM) geospatial data to model blast wave propagation and estimate the damage level of the buildings based on estimated overpressure. The OSM data were simplified, removing architectural details, effectively creating perfectly smooth and cuboidal obstacles to represent buildings. Despite accelerating modelling and hardware capabilities, numerical blast modelling approaches are usually limited by cell size, which greatly limits the ability to represent intricate geometries. Numerical analysis of blast wave propagation at a city scale is computationally demanding due to the large size of the fluid domain; hence, the level of represented structural details is limited to only the most relevant features [24]. As such, architectural details and complex geometries that give the building surfaces a degree of "roughness" are typically not accounted for. While it is often necessary and more computationally efficient to assume simplified geometries, previous studies have not directly investigated the consequences of neglecting/simplifying geometry details or to what extent this potentially modifies the resulting blast wave propagation behaviour.

This study aims to understand the blast wave propagation influenced by the grain siloes during the 2020 Beirut explosion through reduced-scale experimental blast testing. This quantified the extent to which the siloes shielded surrounding areas from the blast wave, helping to resolve the debate surrounding the effectiveness of the siloes in mitigating the impact of the explosion [1]. Furthermore, with advancing computational capabilities and the emergence of studies modelling blast effects at increasingly large city scales, the influence of obstacle geometry details was fur-

ther explored to determine its significance on loading across both experimental trials and numerical models.

2 Methodology

2.1 Experimental design

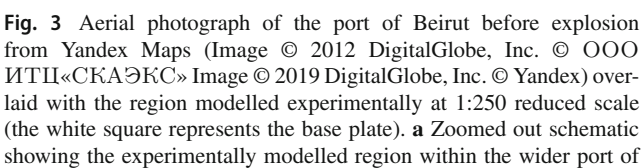
All experiments were performed at the BISRU blast chamber at the University of Cape Town (UCT), South Africa, at a reduced geometric scale of 1:250 to model the Beirut explosion and subsequent blast wave propagation and interaction with the grain siloes obstacle. This scale factor was selected based on the practical range of charge masses that can be detonated at UCT. This scale represented the immediate surroundings near the explosion (within 350 m) to explore the blast interaction and shielding effects surrounding the siloes obstacle (Fig. 3).

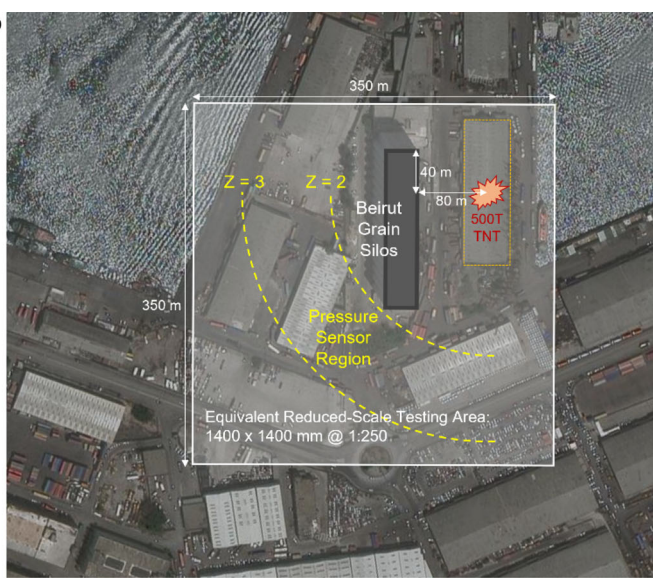
Using estimated values for the explosive yield found by Rigby et al. [1] and Dewey [5], the experimental tests were modelled to represent a 0.5-kt TNT hemispherical surface burst detonation. With a reduced geometric scale of 1:250, an experimental charge mass of 32 g TNT and subsequently 26.7 g of PE4 (which contains 88% RDX mixed with a plasticizer [26]) were used based on Hopkinson–Cranz scaling [15, 16] and TNT equivalence of 1.20 for PE4 [27].

All experiments were performed on top of a $1400 \times 1400 \,\mathrm{mm}$ square base plate, constructed from mild steel with 20 mm thickness, providing a rigid reflective surface representing ground level. This reduced-scale testing area represented a $350 \,\mathrm{m} \times 350 \,\mathrm{m}$ zone at full scale, comprising the explosive detonation in warehouse Hangar 12, the grain siloes structure, and the local surrounding region behind the siloes (Fig. 3b). In reality, there did not appear to be large









Beirut and surrounding city. The blue curve indicates the R=450 m radius at which siloes shielding effects are reported to have ceased [8]. **b** Zoomed-in schematic illustrating the assumed layout of the grain siloes and detonation point at full-scale with overlaid experimental pressure sensing regions defined within the yellow curves denoting blast scaled distances Z=2 and Z=3

topography variations nor dense distribution of obstacles on the blast propagation path, within the area of interest, that would significantly influence the blast wave. Similarly to Leconte et al. [28], the soil was assumed to act as a rigid surface that reflects all incident energy, and therefore, the only energy dissipation to occur was that with increasing distance as the blast propagates away from the centre of the explosive.

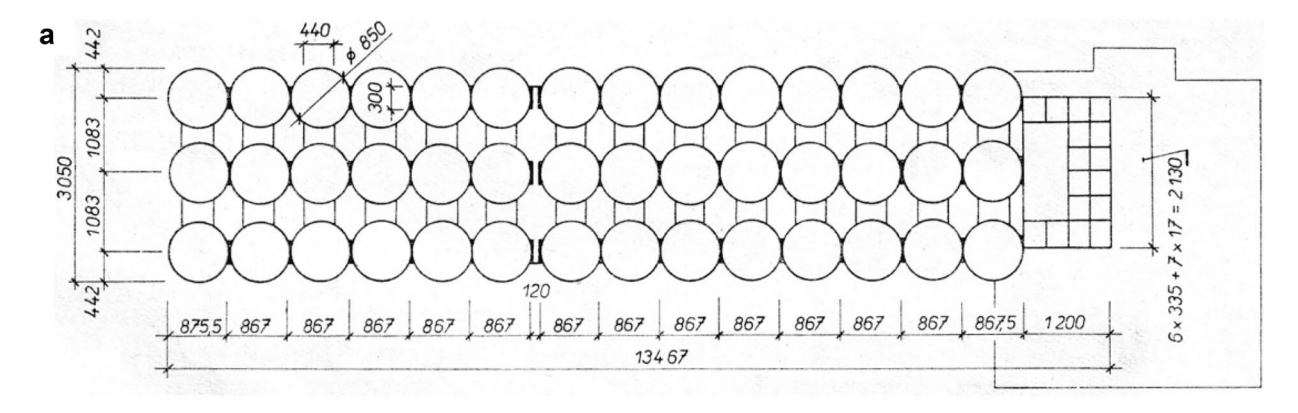
The detonation point and grain siloes structure were arranged on the base plate such that blast overpressure histories could be examined in two key regions of interest, i.e., directly south of the detonation and the shielded region behind the siloes (Fig. 3). The centroid of the explosion epicentre/detonation point was idealised as a single point within the warehouse adjacent to the grain siloes. The stand-off distance between the theoretical detonation point and siloes was 320 mm, representing 80 m onsite, which was considered feasible by Temsah et al. [3] and Forensic Architecture [29]. The location of the explosive was an offset from the northern elevation of the modelled siloes by 160 mm (40 m onsite) (Fig. 3), following forensic studies of the event [4, 6, 29].

Prior to the explosive event, the grain silo structure contained 48 cylindrical siloes, each with an inner diameter of 8.50 m, a wall thickness of 170 mm, and height of approximately 48 m [1] (Fig. 4). Arranged into three rows (of 16) and axially offset by 2.16 m, the walls of the 48 cylindrical siloes intersected [1].

In this study, experiments examined two scaled down representations of the siloes structures, both of which are considered rigid, in reference to the building schematics of the siloes from Temsah et al. [3] in Fig. 4:

- (a) "Rectangular", where the siloes are idealised as a simple cuboid obstacle (Fig. 5a). The rectangular siloes were constructed from 12-mm-thick S355 grade steel plates, forming a cuboid with outer dimensions $609 \times 122 \times 231.2$ mm, which was placed into a 10 mm locating slot in the base frame. The set model on the frame represented the outer edge dimensions of $152.25 \times 30.5 \times 55.3$ m for the siloes. The entrance feature that extends 85 m above the main structure of the silo (labelled feature A in Fig. 4) was omitted for this simplified model.
- (b) "Accurate", where the obstacle was designed to closely represent the outer geometry of the original siloes (Fig. 5b). The accurate siloes obstacle consisted of 32 cylindrical structures, using standard size steel pipes with an inner diameter of 30 mm, outer diameter of 34 mm (i.e., thickness of 4 mm), and a height of 203 mm, which were mounted to an inner steel cuboid structure. Details observed in Fig. 4, including feature A, were constructed from S355 grade steel to the appropriate thicknesses shown in Fig. 5b.





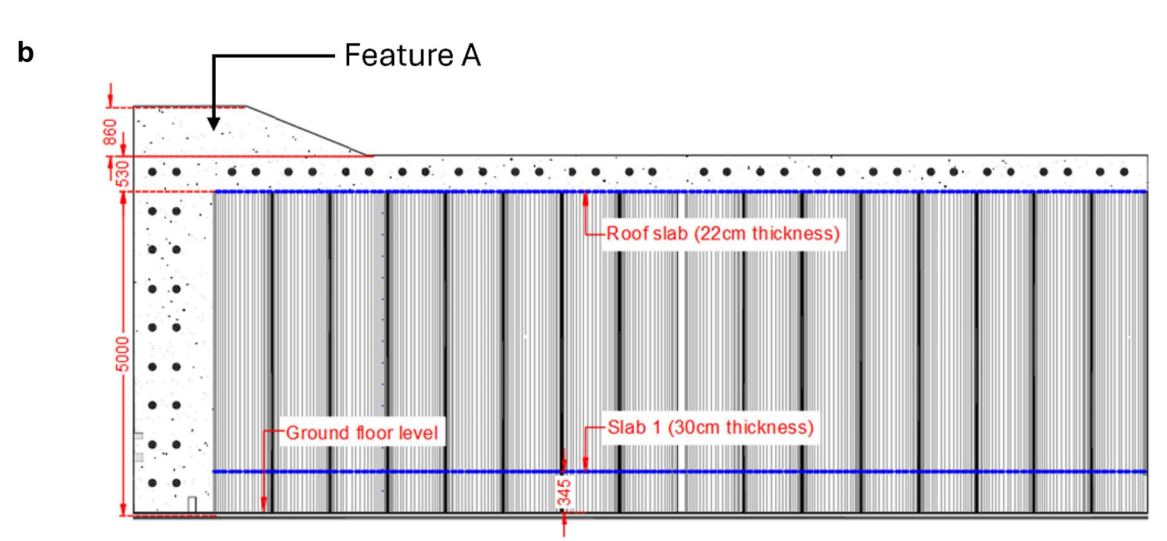


Fig. 4 a Plan dimensions for the grain siloes (cm) and b elevation dimensions of the grain siloes (cm) from Temsah et al. [3]

2.2 Experimental program

Explosive charges were shaped into 26.7-g hemispheres of PE4 using a 3D-printed mould and were placed on a sacrificial plate on the steel base plate to simulate a surface explosion. The experimental setup was placed in the centre of the BISRU blast chamber, at least 1 m away from the walls to avoid wall reflections interfering with the initial pressure histories recorded at all sensor locations.

Similar to the approach taken in [30], the repeatability and reliability of the unobstructed (free-field) loading were assessed first, such that any trends in the siloes obstacles tests can be attributed to genuine blast–obstacle interaction behaviour rather than experimental spread or other underlying uncertainties. The three testing arrangements are shown schematically in Table 1, and images of the as-built siloes obstacles are shown in Fig. 6.

The base plate was instrumented with piezoelectric pressure sensors (PCB Piezotronics GmbH 113B series, details of the specifications can be found in [13, 31]), in 12 unique

radial locations surrounding the siloes obstacle, at a blast scaled distance of either $Z = 2 \,\text{m/kg}^{1/3}$ or $Z = 3 \,\text{m/kg}^{1/3}$ (see Fig. 7), in one of three categories (Table 2):

- Downstream exposed/reflected: Y, B, those directly exposed to the explosive. The B locations are in line with the front face of the building.
- Partially shielded: C, partially behind the obstacle and in line with the explosion.
- Shielded: X, E, D, those located directly behind the obstacle.

The pressure sensors were mounted flush within the base plate (see Fig. 6). A polymer housing was used to minimise vibrational effects from the base plate as the explosive is detonated at ground level. Pressure data were recorded at a sampling frequency of 2 MHz, and recordings were synchronised with the detonation using a break-wire positioned beneath the charge, formed of a thin metal foil connected to an electrical circuit that triggers a voltage response as the foil breaks, signalling data capture on the data acquisition system. The data acquisition system (HBK Genesis HighSpeed



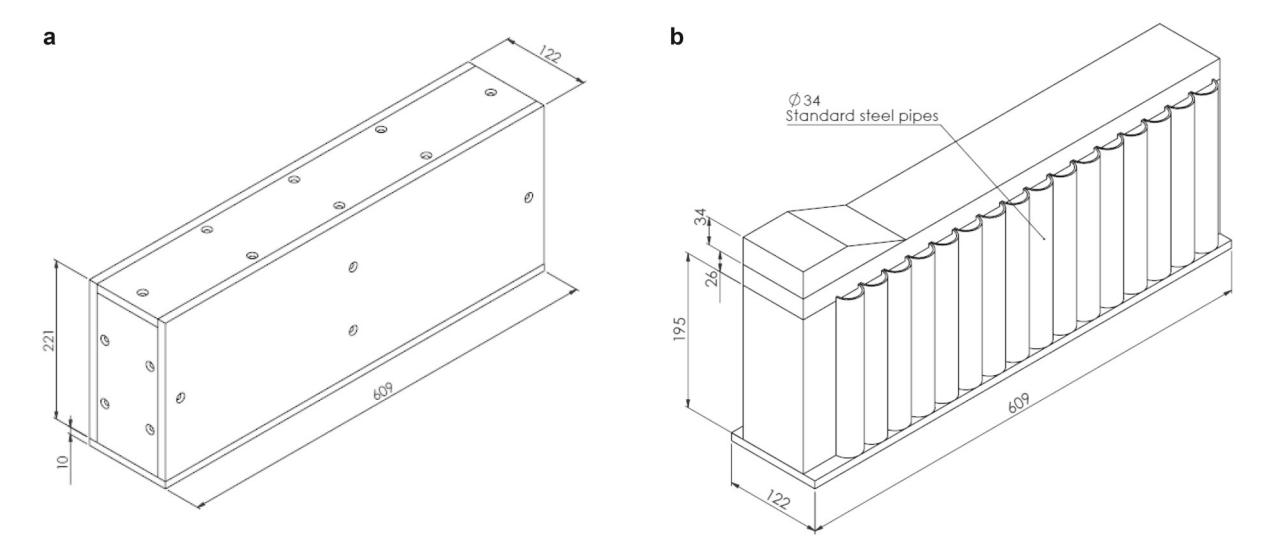
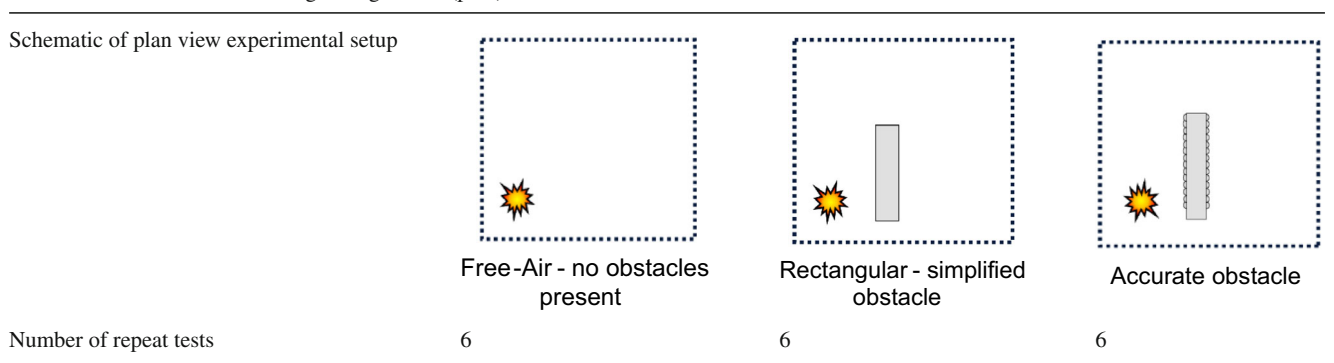


Fig. 5 Beirut grain siloes obstacles were constructed from steel components at two geometric fidelities for reduced-scale experiments: a rectangular siloes obstacle ($609 \times 122 \times 231$ mm), b accurate siloes obstacle with closer resemblance to the Beirut grain siloes

Table 1 Schematics of the testing arrangements (plan)



Tethered Mainframes Gen2tB) permitted eight inputs, one of which was reserved for the triggering mechanism. Limited by seven pressure sensing channels, sensors were shared between the different locations although measurements were captured at B sensors (in line with the front face of the building) in every test.

2.3 Numerical methodology

Viper::Blast [32] (version 1.20.8) was used to perform computational fluid dynamics (CFD) analyses of both series of experimental tests including the a) rectangular (simplified) and b) accurate siloes obstacle. The basic functionality of Viper::Blast is based on the methodology described by Rose [33] and uses the AUSMDV numerical scheme as described by Wada and Liou [34] to solve the inviscid Euler equations.

Numerical models were undertaken in a single-stage using a three-dimensional (3D) modelling domain to simulate the surface detonation of the explosive charge, subsequent blast wave propagation, and interaction with the siloes obstacle. The steel siloes structures used in the experiments were modelled as obstacles within the 3D domain, which itself was filled with air modelled as an ideal gas to have an ambient pressure of 101.3 kPa through specifying the adiabatic constant, $\gamma = 1.4$, air density, $\rho = 1.225 \text{ kg/m}^3$, and initial internal energy, $e = 2.068 \times 10^5 \text{ kJ/kg}$ (Table 2).

A single cuboid obstacle was specified for the simple siloes model, whereas the accurate siloes structure was constructed from a combination of cuboid, cylindrical, and trapezoidal obstacles with outer dimensions and arrangements consistent with the experiments (Fig. 8). By default, obstacles in Viper::Blast have fully reflective boundary conditions, thus modelling a perfectly rigid structure with reflective surfaces. A reflective boundary condition was assigned to the lower *z*-plane of the 3D domain to model the tabletop surface in the tests, and transmissive boundary conditions were assigned to all other domain boundaries to model free-field (unobstructed) blast wave propagation.

TNT material was specified at the location of the explosive charges in the experiments within a 3D domain containing



Fig. 6 Photographs of the experimental setup for the siloes obstacle arrangements for the a rectangular and b accurate scenarios

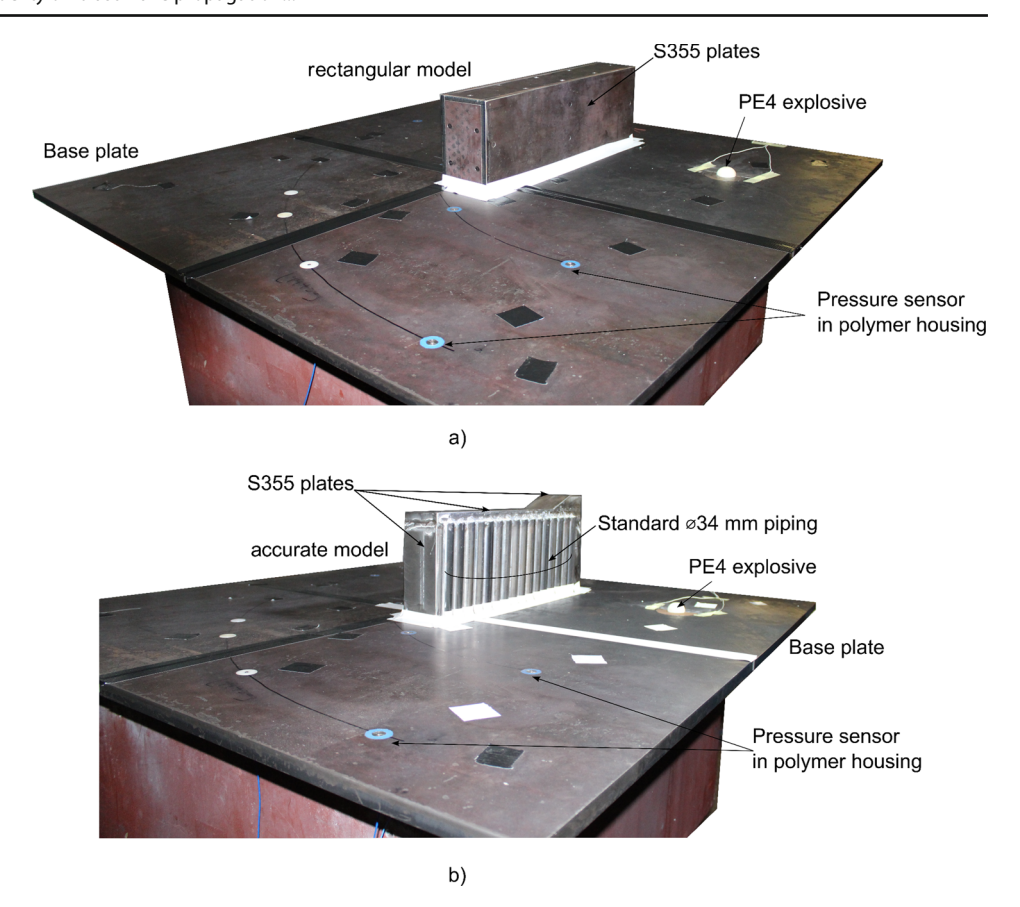


 Table 2
 Summary of pressure gauge details and locations within the experimental setup

Label	Sensor device	Z (m/kg ^{1/3})	Terminology/Location description	Coordinates <i>X</i> , <i>Y</i> (relative to the detonation point) in mm (see Fig. 7)
0	_	_	Reference: explosive detonation point	0, 0
X2	113B27	2	Horizontal in line with explosive, close proximity to building	640, 0
X3	113B28	3	Horizontal in line with explosive	960, 0
Y2	113B27	2	Vertical in line with explosive	0, 640
Y3	113B21	3	Vertical in line with explosive	0, 960
B2	113B27, 113B21	2	Vertical in line with front face of building, close proximity to building	330, 550
В3	113B28	3	Vertical in line with front face of building	330, 900
C1	113B27	3	In line with bottom sidelfront face corner	560, 770
C2	113B27	3	In line with bottom sidelback face corner	780, 580
D2	113B27	2	Line midway between C1 and X, close proximity to building	560, 320
D3	113B27	3	Line midway between C1 and X	830, 470
E2	113B27	2	Line midway between D and X, close proximity to building	630, 170
E3	113B28	3	Line midway between D and X	930, 250



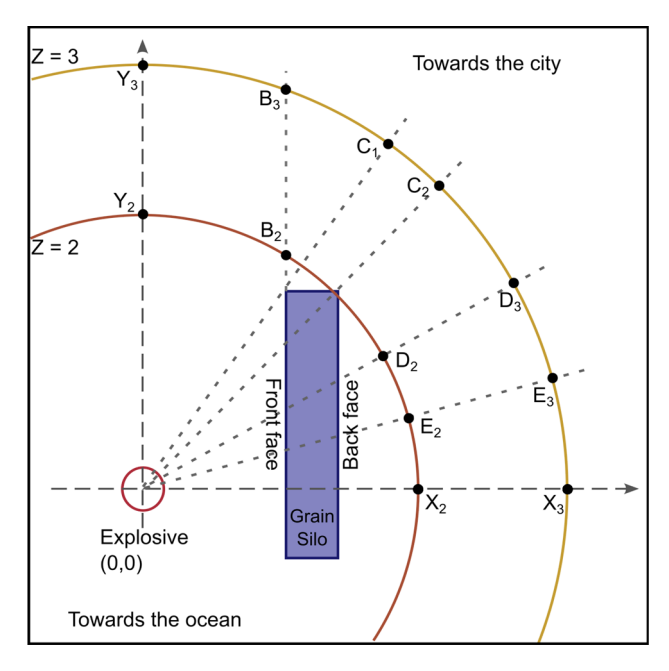
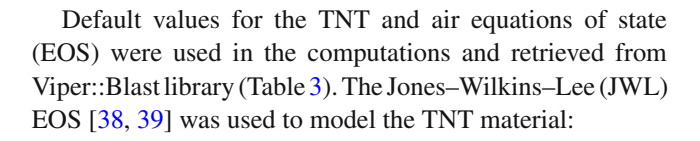


Fig. 7 Plan view schematic showing pressure gauge locations—Note that the schematic was rotated from Fig. 3

elements of atmospheric air. Care was taken to closely replicate the hemispherical charge shape and influence of the detonator used in the experiments, while also accounting for the surface burst condition due to positioning on the steel tabletop. A spherical charge, constructed from TNT material, was positioned intersecting the lower z-plane domain boundary (i.e., z=0) to model the hemispherical charge geometry.

The gross explosive charge mass tested in experiments (26.7 g PE-4) was scaled to an equivalent mass of 32.04 g TNT, assuming a TNT equivalence of 1.2 for PE4 [24, 29, 30]. The gross TNT equivalent charge mass was increased by 2.36 g TNT, representing the contribution from the 1.42 g pentaerythritol tetranitrate (PETN) L2A2 detonators used in experiments, assuming a TNT equivalence of 1.66 for PETN [36]. While the Viper::Blast manual suggests doubling the charge mass to model a surface burst scenario, improved agreement was observed using a lower factor of 1.8 according to Unified Facilities Criteria (UFC) guidance [35, 37]. The reduced reflection factor accounts for the tabletop not being perfectly reflective and some energy losses occurring, and it is important to note that this approach is considerably less computationally intensive than setting the charge mass as the true value, modelling the ground as a compressive medium, and coupling the two. The experimental gross mass (34.4 g TNT) was therefore multiplied by 1.8, yielding a final (net equivalent) TNT charge mass of 62 g. For a specified density of 1540 kg/m³ for TNT, the modelled 62 g charge had a radius of 21.262 mm.



$$p = A\left(1 - \frac{\omega}{R_1 V}\right) e^{-R_1 V} + B\left(1 - \frac{\omega}{R_2 V}\right) e^{-R_2 V} + \frac{\omega}{V}e.$$
(1)

In (1), p denotes pressure and V and e are the specific volume and specific internal energy of the explosive, respectively. Parameters A, B, R_1 , R_2 , and ω are constants evaluated through experiments for any high explosive material. For the TNT material, values for these parameters were taken from the Viper::Blast built-in material library and are listed in Table 3.

The multi-material solver method 4 (JWL with afterburn) was used to model both the detonation of the explosive material and subsequent shock wave propagation through air. This solver includes a programmed burn model and a Jones–Wilkins–Lee (JWL) equation of state to enable modelling detonation of the charge and detonation products along with an additional afterburn component. This solver was specified for increased accuracy, particularly as a large extent of the blast wave propagation examined in this study can be considered as near field ($Z < 2 \text{ m/kg}^{1/3}$) [37], and therefore, in close proximity to the explosion fireball.

Viper::Blast models using solver method 4 require the entire modelling domain to fit on the computer's graphics processing unit (GPU), meaning that the total model size (number of cells) and cell size (hence resolution), are limited by hardware capacity. An iterative process was adopted to minimise computational expense through efficient domain sizing while ensuring sufficient surrounding space to avoid potential interference at domain boundaries from affecting pressure measurements. The final 3D modelling domain had outer dimensions, 1.5 m \times 1.5 m \times 0.6 m.

Pressure monitoring points were assigned at 4318 locations (Fig. 9) in the domain using 3D Cartesian coordinates. This provided a dense pressure measurement zone within blast scaled distances $2 \text{ m/kg}^{1/3} < Z < 3 \text{ m/kg}^{1/3}$, i.e., 640 mm < R < 960 mm, where R is the stand-off distance from the detonation point. This measurement zone is consistent with the heat map approach subsequently used to analyse the experimental data and overlaps all experimental pressure sensor locations.

A grid sensitivity study was undertaken to examine the influence of mesh size on accuracy of the 3D models. In Viper::Blast, a Cartesian mesh with uniformly sized cubeshaped cells is specified throughout the entire domain. For each obstacle geometry (rectangular or accurate siloes), three cell sizes were examined (Table 4).



Table 3 Parameters used for modelling air and PE-4

	Air	TNT
Equation of state (EOS)	Ideal gas	JWL
Initial conditions	$\gamma = 1.4$	$A = 3.712 \times 10^5 \text{ MPa}$
	$e = 2.068 \times 10^5 \text{ kJ/kg}$	B = 3.231 GPa
	$\rho = 1.225 \text{ kg/m}^3$	$R_1 = 4.15$
		$R_2 = 0.95$
		$\omega = 0.3$
		$\rho = 1540 \mathrm{kg/m^3}$

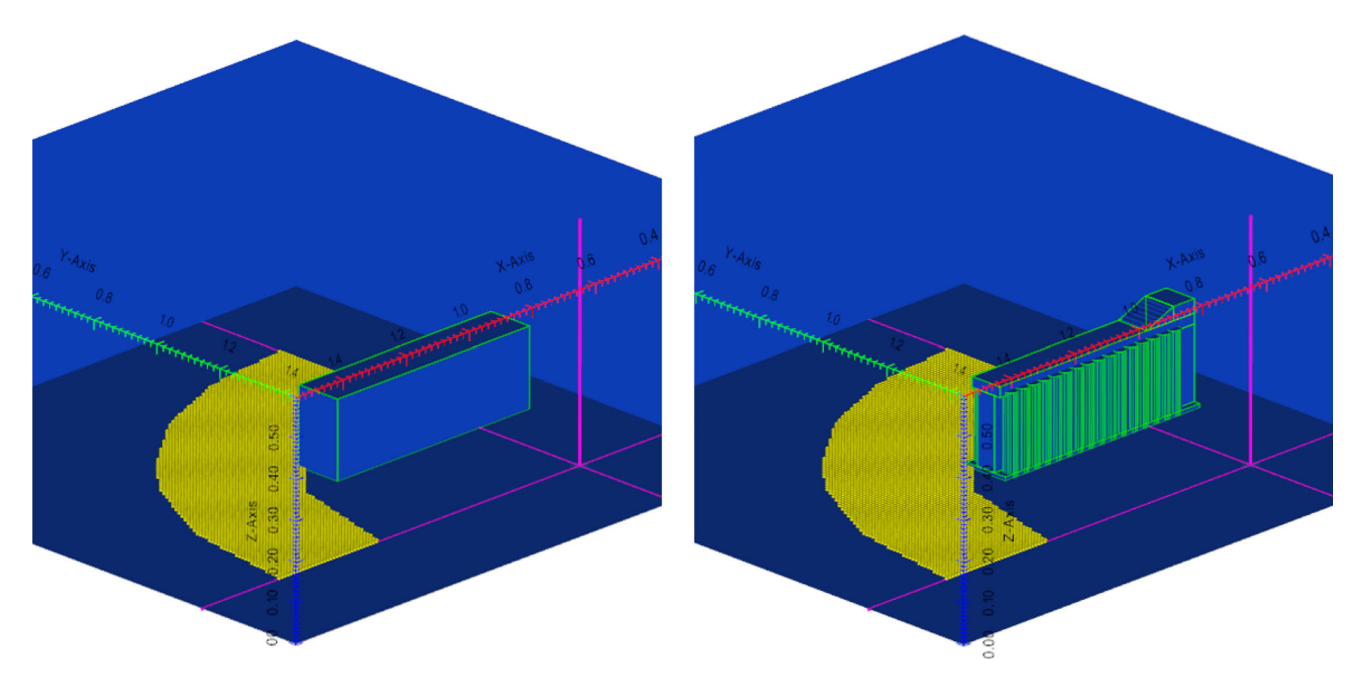


Fig. 8 Isometric view of 3D CFD modelling domain in Viper:Blast containing the rectangular (left) and accurate (right) siloes obstacles with yellow markers indicating positions of pressure monitoring locations

Fig. 9 Plan view of 3D CFD modelling domain in Viper:Blast containing the simple rectangular (left) and accurate (right) siloes obstacles and extensive pressure monitoring region

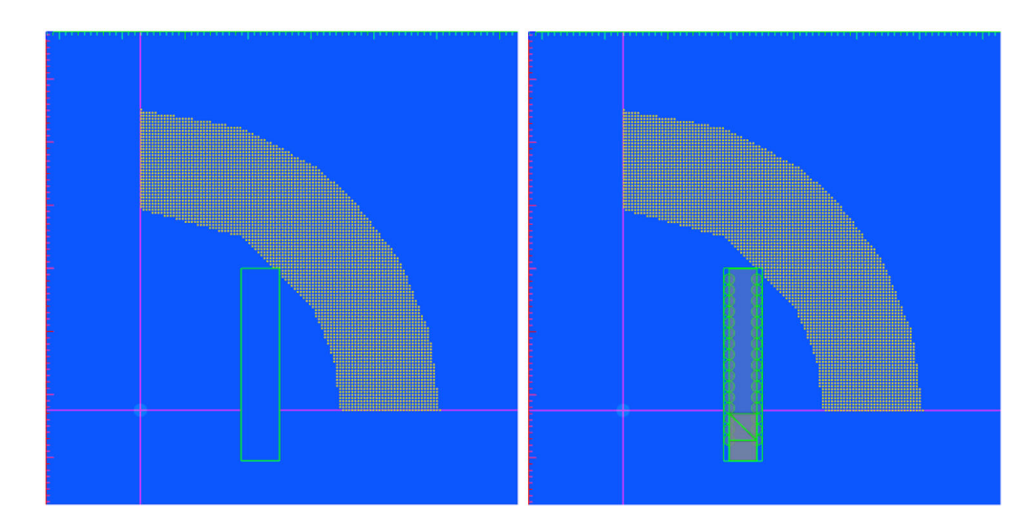




Table 4 CFD domain cell size sensitivity study (5, 3, and 2 mm cells)

Model	Cell size (mm)	Total no. of cells	Simulation run time
Rectangular siloes	5	1.0800×10^7	15 min 36 s
	3	5.0000×10^7	1 h 41 min
	2	1.6875×10^{8}	6 h 11 min
Accurate siloes	5	1.0800×10^{7}	18 min 26 s
	3	5.0000×10^7	1 h 29 min
	2	1.6875×10^{8}	12 h 58 min

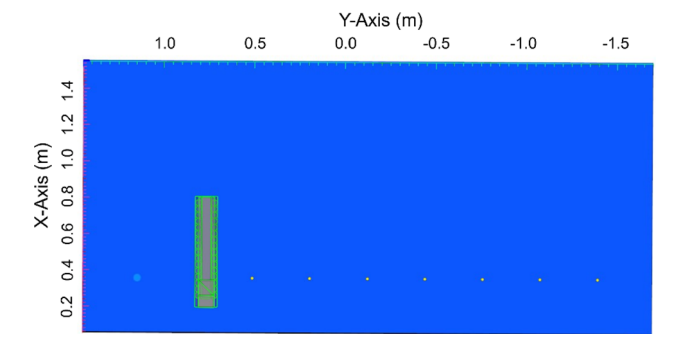


Fig. 10 Extended numerical modelling domain with additional pressure gauges to examine siloes shielding effects further afield

Each model was simulated for a total time of 4.0 ms, which allowed sufficient time for the primary blast wavefront to propagate around the siloes and pass the furthest measurement locations. Pressure data were extracted at time increments of 0.001 ms; this provided good resolution of pressure histories while maintaining manageable data storage. Simulations were run on a Dell Alienware Aurora R11 workstation (Intel(R) Core(TM) i9-10900KF @ 3.70 GHz CPU) with 64 GB RAM and NVIDIA GeForce RTX 3080 Ti 12,287 Mb graphics card.

Two additional models were created to examine the siloes' shielding behaviour at greater distances beyond those examined experimentally. An extended 3D modelling domain was specified (1.6 \times 3.142 \times 0.6 m) to obtain pressure measurements in the shielded zone (behind the siloes) with a series of pressure gauges specified at ground level ($z=0\,\mathrm{mm}$) at incremental distances corresponding to blast scaled distances 2 m/kg^{1/3} < Z < 8 m/kg^{1/3} (Fig. 10). Utilising the same methodology as previously described, the free-field case (no siloes obstacle) as well as the rectangular and accurate siloes cases were simulated using a cell size of 5 mm, yielding a total of 2.264×10^7 cells.



3.1 Experimental results

3.1.1 Free-air trials

Presented in Figs. 11a, b and 12a, b are pressure histories (more specifically, overpressure and specific impulse) recorded at $Z = 2 \text{ m/kg}^{1/3}$ (10 traces) and $Z = 3 \text{ m/kg}^{1/3}$ (14 traces), respectively, along with the predictions using the Kingery and Bulmash (KB) empirical formulae. The overall trends qualitatively agree, with some differences, for recordings at both scaled distance positions. It is important to note that the data presented in the aforementioned figures are the result of four individual trials where gauge data were recorded at the same radial distance away from the charge but at different polar coordinates. This means that variability in readings could also be attributed to any non-perfectly spherical expansion of the fireball and shock wave. Tyas [40] discussed three distinct regions as a result of empirical explosive characterisation trials in which data within the scaled distance region of $1 \text{m/kg}^{1/3} < Z < 3 \text{ m/kg}^{1/3}$ exhibit larger spreads in output parameters as a direct result of Richtmyer-Meshkov (RM) and Rayleigh-Taylor (RT) fluid dynamic instabilities, with blast parameters measured outside of this region exhibiting much greater consistency [35, 41]. The fact that the data presented exhibit qualitative inconsistencies, particularly at $Z = 2 \text{ m/kg}^{1/3}$, for arrival time and peak overpressure, with reduced variation at the $Z = 3 \,\mathrm{m/kg^{1/3}}$ positions, agrees with the aforementioned hypothesis as reported by Tyas [40], as well as Bogosian, Ferrito, and Shi [42].

Both the specific impulse and the time duration parameters are however considerably lower than semi-empirical predictions; a finding similar to incident gauge results presented by Farrimond et al. [35], who conducted explosive yield characterisation for a number of plastic explosives and concluded this to be a result of inaccuracies in the predictions themselves, due to the remarkable comparison between reflected measurements and predictions from the same trials. This behaviour was also recorded by Rigby et al. [30], whereby both reflected peak pressure and impulse



Fig. 11 Ten pressure histories from a 26.7-g PE4 hemispherical charge at $Z = 2 \,\mathrm{m/kg^{1/3}}$ with the empirical predictive methods' fits overlain: a overpressure and b specific impulse

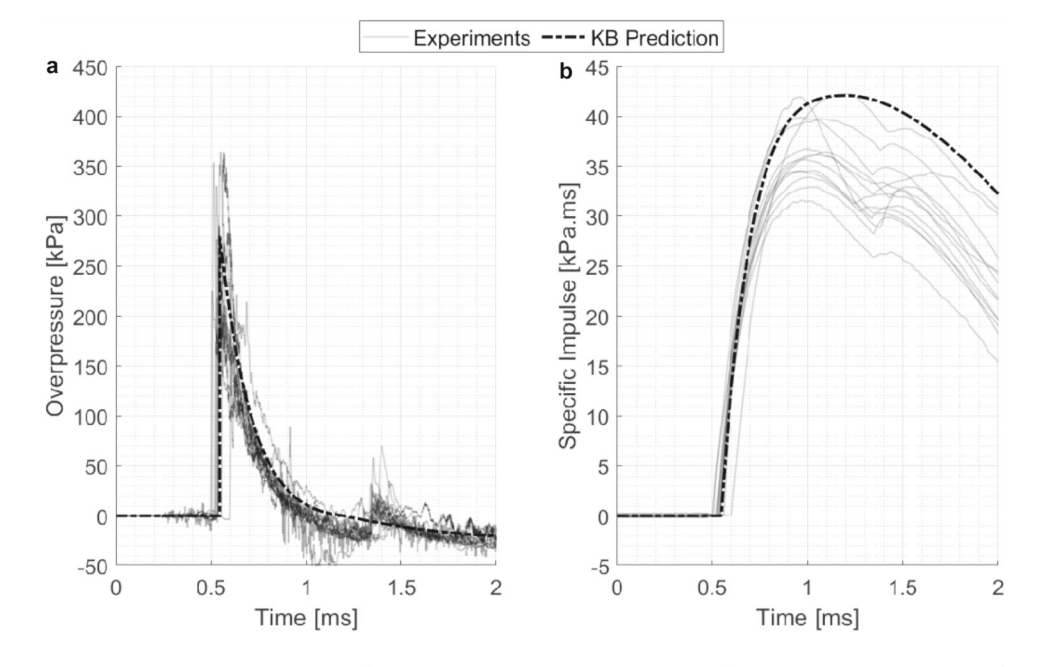
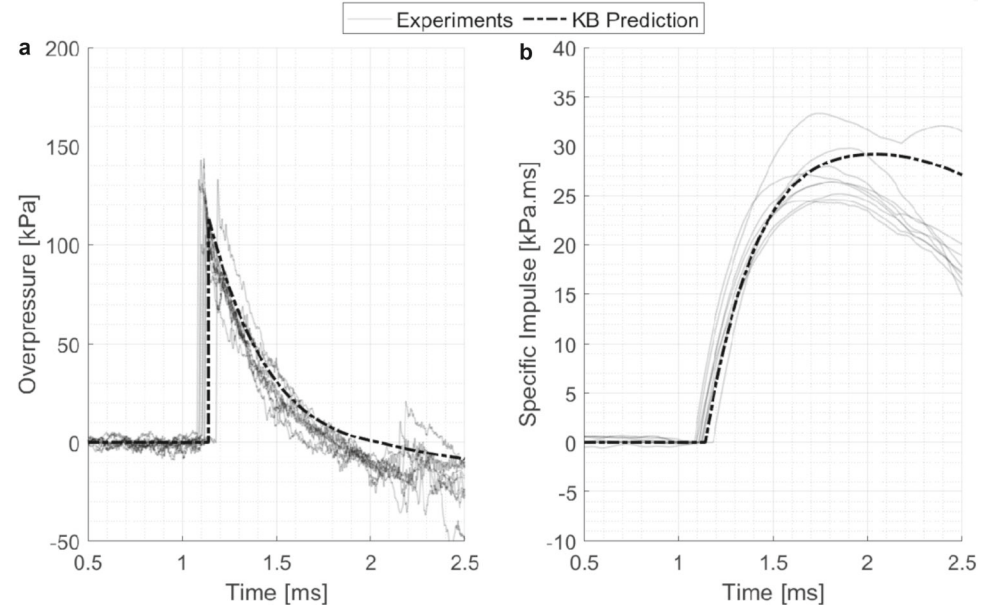


Fig. 12 Fourteen pressure histories from a 26.7-g PE4 hemispherical charge at $Z = 3 \,\text{m/kg}^{1/3}$ with the empirical predictive methods' fits overlain: **a** overpressure and **b** specific impulse



and incident free-air peak pressure values generally agree with the KB predictions, but incident impulse recordings were significantly lower. Markers in Fig. 13a–d have been set as partially transparent to allow variations in the compiled data set to be visualised. Here, areas with seemingly darker markers indicate a greater degree of overlap and hence higher consistency in the measurements. It can be seen that the processed data compare well with predictions, therefore giving confidence in the methodology used in the remainder of this article, as well as providing a benchmark data set to compare to.

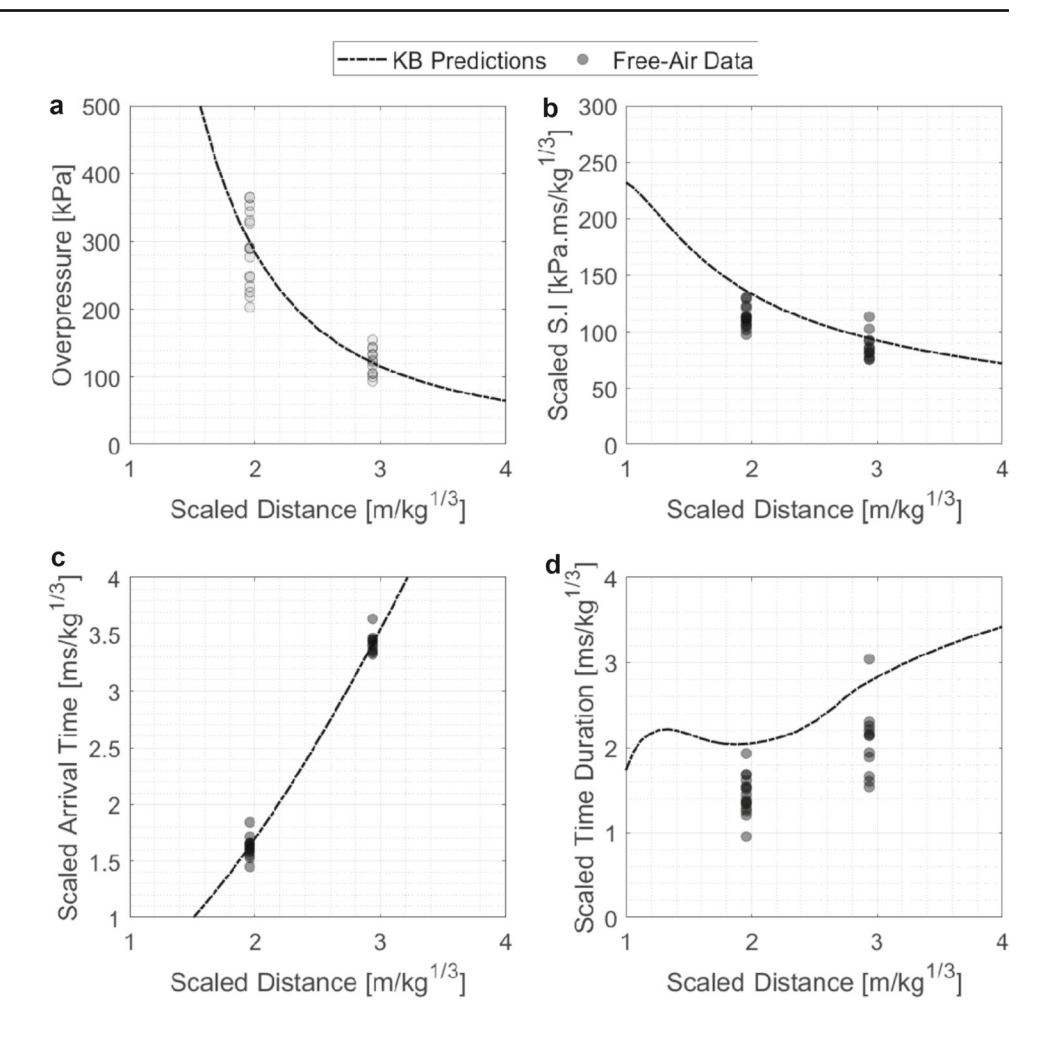
3.1.2 Rectangular silo trials

When considering obstacle fidelity effects on blast loading, establishing the loading conditions as a direct result of a rectangular silo obstacle represents the most fundamental interaction case for the Beirut blast. Pressure histories were recorded at identical positions to the free-air trials and compared directly to highlight key blast wave features as a result of reflections, diffraction, and shielding.

Figure 14 shows the pressure history profiles for each gauge, compared against the KB predictions. In the unobstructed locations (gauges Y2 and Y3) in Fig. 14, it can be clearly seen that the incident pressure and arrival time are



Fig. 13 Compiled blast parameters from hemispherical PE4 explosive trials as a function of scaled distance, which has been scaled to a 1-kg TNT equivalent hemispherical charge (assuming a TNT equivalence of 1.2 for PE4), and compared with KB predictions: a peak overpressure, b scaled peak specific impulse (SI), c scaled arrival time, and d scaled positive phase duration



almost identical to that of the prediction curve, expected as an obstacle will not influence this original expansion. However, within the positive phase is the arrival of a reflected wave from the front face of the obstacle, causing a second pressure peak and increasing the evaluated specific impulse.

Within the diffracted case locations (gauges B2 and B3) in Fig. 14, a definitive clearing-like behaviour is present within the positive phase, aligning with the theory which suggests a rarefaction wave is relieving the loading when interacting with finite-sized targets. Interestingly in this case, the reflection from the wall arrives at a similar time to the incident wave, causing a coalescence of waves and resulting in much higher overpressures to be experienced. These two conflicting influences on the loading result in a net preservation of the overall specific impulse within the positive phase of the event when compared to a free-air scenario; however, the loading from the obstacle occurs over a shorter duration.

Finally, considering the fully shielded experimentally recorded positions (gauges E2 and E3) in Fig. 14, the representative pressure history directly behind the rectangular silo shows significant reductions in the incident pressure with the coalescence of multiple diffracted waves

of low magnitude arriving near-simultaneously. For E3 in Fig. 14, the measured pressure history downstream of the obstacle at $Z=3\,\mathrm{m/kg^{1/3}}$ begins to behave like a normal free-air wave with a delayed arrival. The distinct changes in waveforms between gauges E2 and E3 suggest a physical process of self-healing is occurring, with the flowfield reverting towards that of a free-air blast. This is a significant finding and suggests that complex shock wave interaction may eventually equilibrate and dissipate and the flowfield return to pseudo-free-air conditions.

To investigate full-field loading behaviours from the experimental data, the authors propose a bespoke interpolation method making use of data recorded in discrete locations from nominally identical trials:

- An average of the extracted positive phase blast parameters at each position was used to provide a "known" baseline value at that given position.
- Each pair of gauges with line of sight of one another were then connected, and a biharmonic interpolation scheme was implemented to estimate the given blast parameter behaviour along each connected line.



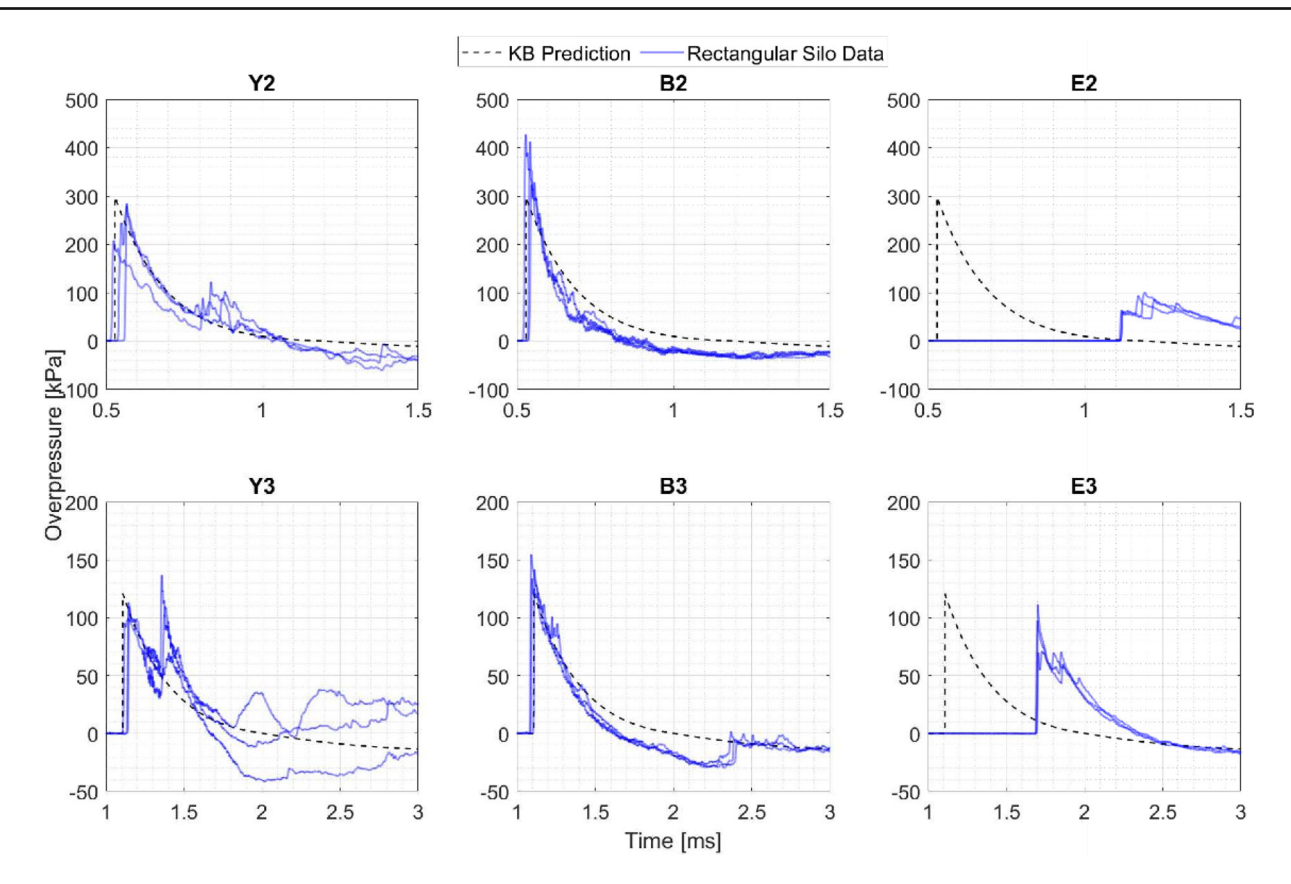


Fig. 14 Overpressure histories expected for free-field propagation (using KB prediction) compared with pressure profiles experimentally measured at locations surrounding the rectangular siloes obstacle

 When lines of sight intersect, the interpolated values at these positions were averaged to inform a more general behaviour across the entire domain in the attempt to minimise errors which may occur from erroneous gauge data.

Figure 15 presents a graphical representation of this interpolation method with its output values for free-air peak overpressure. Clearly seen is a radial decrease in pressure as stand-off distance increased from the charge centre with values at $Z = 2 \,\mathrm{m/kg^{1/3}}$ being approximately 290 kPa and KB predictions 283 kPa and for $Z = 3 \,\text{m/kg}^{1/3}$ being approximately 120 kPa and KB predictions being 115 kPa. When making comparisons between the predicted full-field behaviours and KB values, on average, there is a maximum of 5% error across pressure, specific impulse, and arrival time throughout the entire domain, which provides confidence in the interpolation method for providing qualitative representations of the propagation behaviour. This agrees fundamentally with the data presented in Fig. 13a–d whereby the extracted parameters agree with KB predictions for freeair incident measurements.

While the utilised interpolation method is not sophisticated enough to definitively represent the complex behaviour

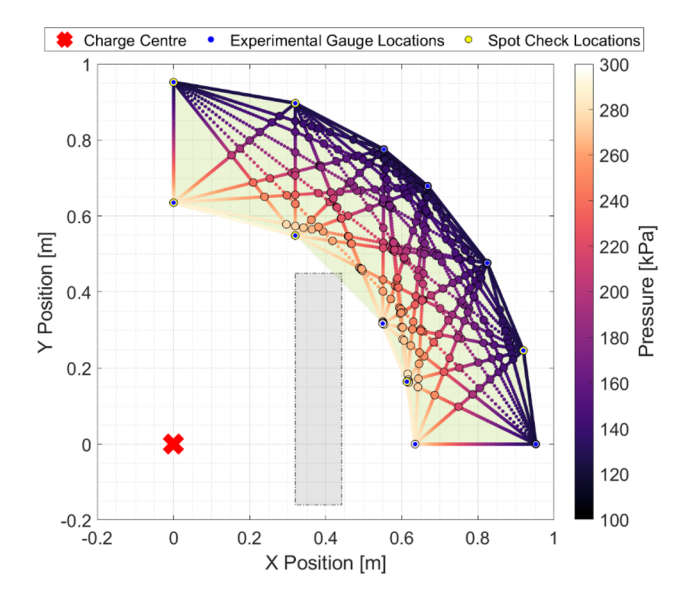


Fig. 15 Graphical representation of the interpolation scheme implemented between known experimental gauges through line of sight and line interaction averaging

of the blast wave's interaction with the silo obstacles, comparisons between the results extracted from free-air trials and those with obstacles in place allow for an investigation into



the amplification and/or reduction behaviours experienced. Presented in Fig. 16 are the interpolated results from the rectangular silo trails normalised by the free-air results, which were processed with an identical methodology. By normalising the data to the free-air results, any errors introduced by the interpolation method were effectively mitigated, allowing the visual plots to clearly show the qualitative amplification or reduction of each positive phase blast parameter resulting from the structural interaction.

Zehil [8] modelled the events of Beirut port explosion using similar simplistic geometries, assuming both a rigid and flat cuboidal structure and a cuboidal explosive shape, and recording blast parameters 1 m above the ground surface. Zehil [8] found approximately 65% and 45% reductions in the overpressure outputs at both $Z=2\,\mathrm{m/kg^{1/3}}$ and $Z=3\,\mathrm{m/kg^{1/3}}$, respectively, whereas in this article, the experimental reductions were approximately 60% and 30%, respectively. Charge shape effects have been identified as

influential on blast parameters across all scaled distances in free-air and simple interaction cases [43]; however, the region of $Z < 4 \,\mathrm{m/kg^{1/3}}$ has been recognised as much more prone to variations [44]. Despite the explosive shape being different and the measurement positions not being at the same height, the magnitudes of loading attenuation are similar, suggesting that downstream shielding characterisation is mainly driven by the scale of the blast with respect to the obstacle it interacts with [45]. The comparable results at $Z = 2 \,\mathrm{m/kg^{1/3}}$ suggest that shape effects of the detonation are somewhat hidden within the complexity and variability of the fluid dynamic instability-corrupted wave interactions.

3.1.3 Accurate silo trials

Similar experimental trials were conducted but with a more geometrically accurate silo model to consider the differences in obstacle granularity and how this affects spatial and tem-

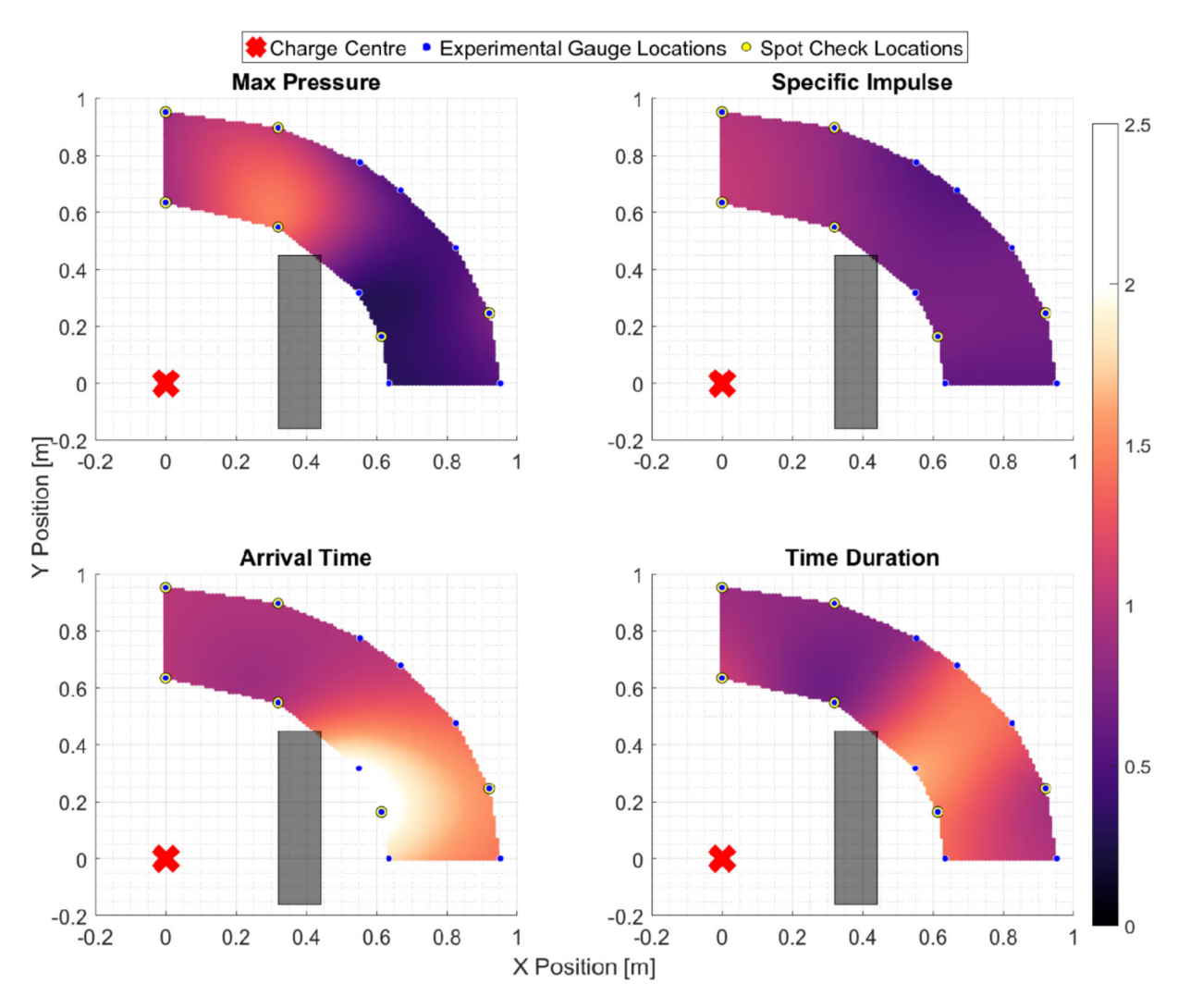


Fig. 16 Normalised heatmaps showing the interpolated results from the rectangular silo experiments normalised by the free air results, showing the spatial distribution of positive phase blast wave parameters



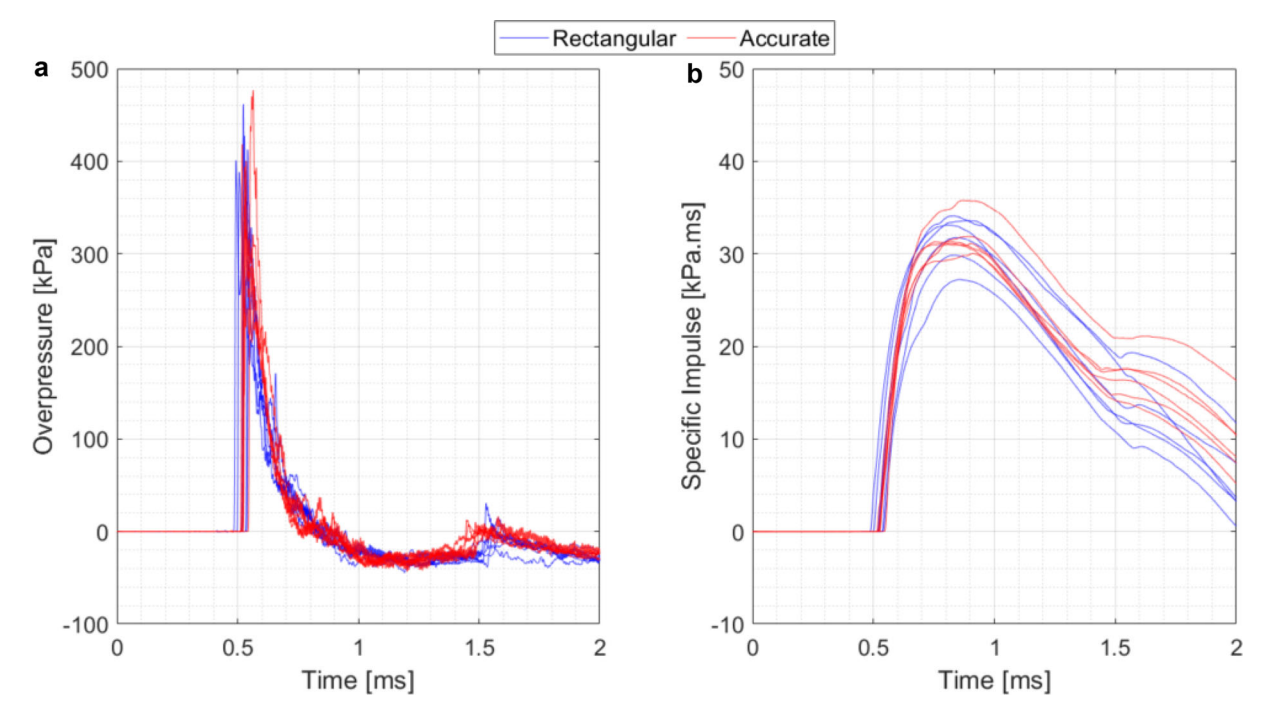


Fig. 17 Compiled pressure histories from a 26.7-g PE4 hemispherical charge at gauge B2 ($Z=2\,\text{m/kg}^{1/3}$) for both the rectangular and accurate geometry siloes: **a** overpressure and **b** specific impulse

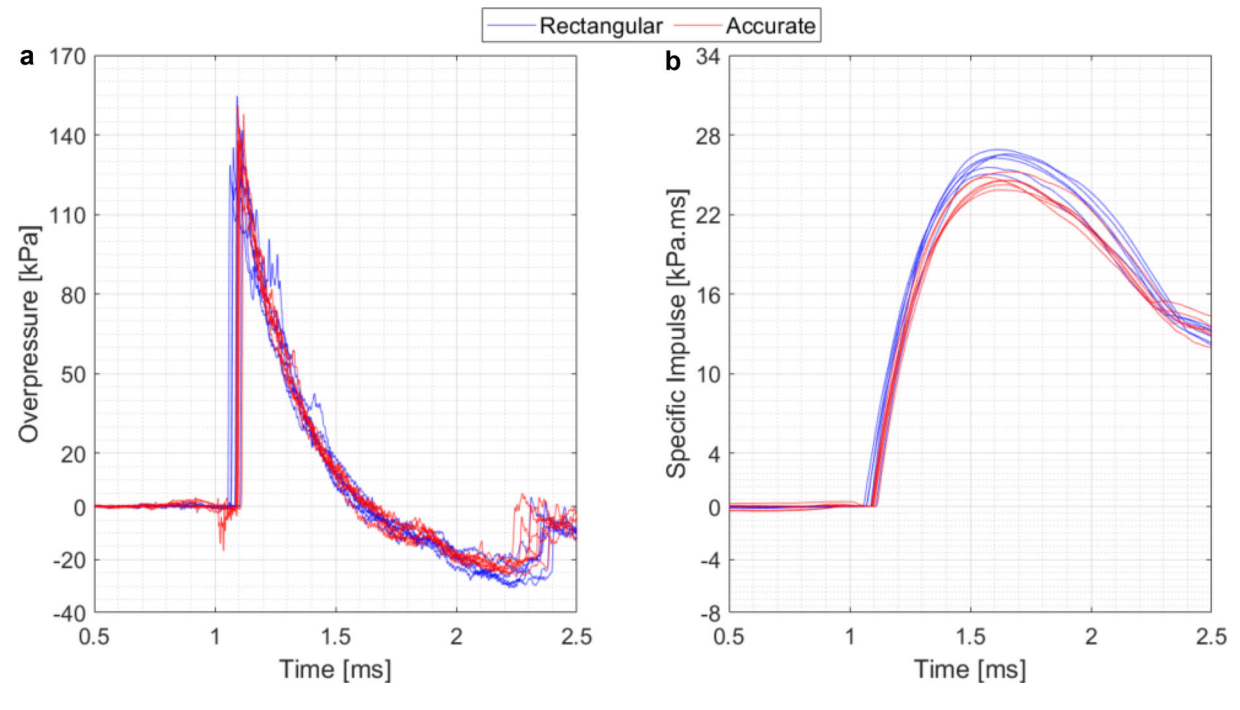


Fig. 18 Compiled pressure histories from a 26.7-g PE4 hemispherical charge at gauge B3 ($Z = 3 \text{ m/kg}^{1/3}$) for both the rectangular and accurate geometry siloes: **a** overpressure and **b** specific impulse

poral loading. Firstly, it was important to compare the gauge recordings at positions B2 and B3, from both the rectangular and geometrically accurate silo trials, to ensure that the comparable data points align on arrival time and peak pressure, with any differences in impulse and duration being directly

linked to differences in the fidelity of the obstacle affecting the clearing wave interaction mechanism.

Figures 17 and 18 show pressure and impulse histories at positions B2 and B3 which represent an area that is definitively affected by clearing, which is governed itself by the



shape and size of the structure the wave interacts with. While the pressure histories are qualitatively similar regardless of obstacle fidelity, there are some key features to highlight. At $Z = 2 \,\mathrm{m/kg^{1/3}}$ in Fig. 17a, b, there are no visible trends regarding the influence of obstacle fidelity, which comes as no surprise based on the commonly discussed increased variability in blast parameters in this region due to fluid dynamic instability formation. Furthermore, Rose et al. [46] reported the effects on pressure and impulse as a result of a protective wall, making comparisons to free-air propagation via percentage change contour plots and showed that in a similar position to that of B2, there is a highly spatially varying impulse from between 40 and 100%, but pressures were somewhat unchanged with values 80–100%, which is similar to that seen in Fig. 16. For this reason, it is difficult to determine whether obstacle fidelity influences parameters within the near field.

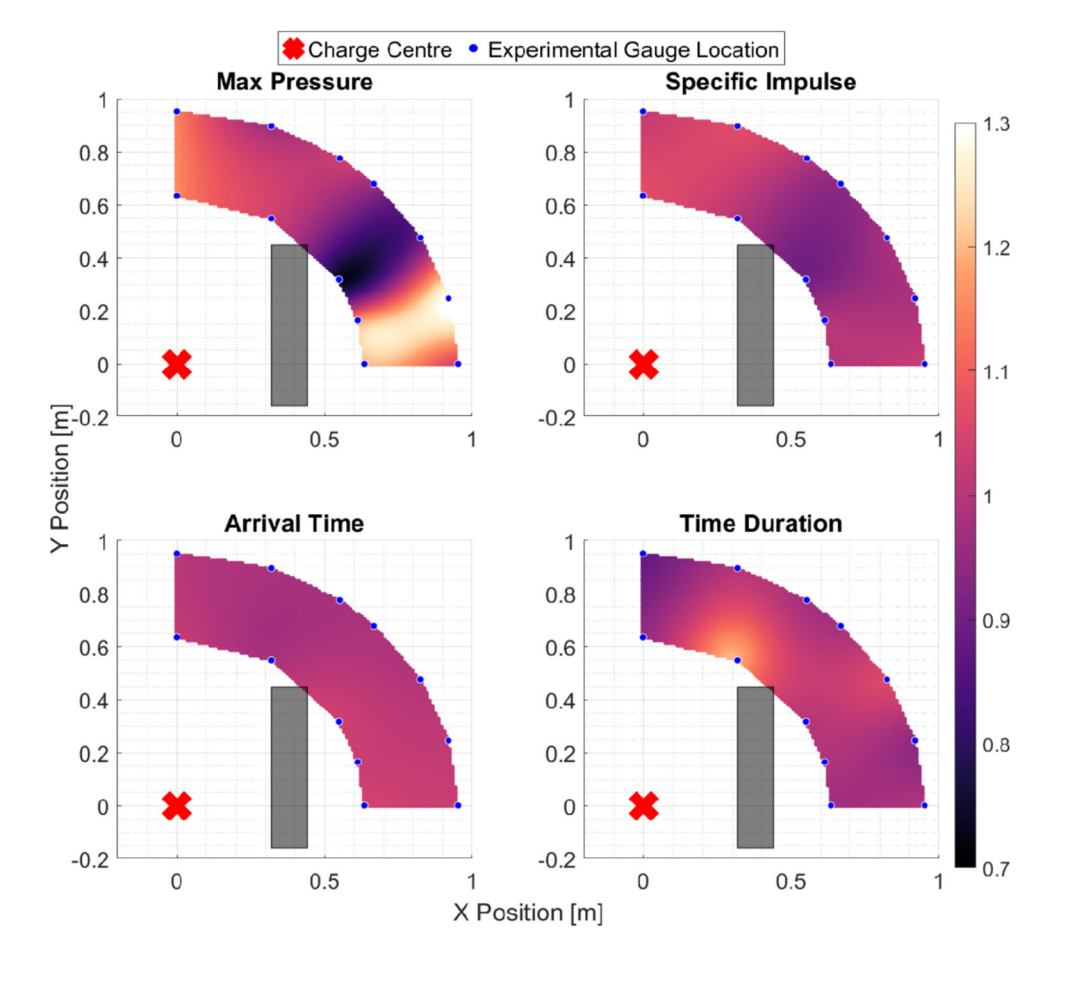
However, at greater distances downstream from an obstacle ($Z=3\,\mathrm{m/kg^{1/3}}$), trends do begin to form and fidelity clearly influences shock parameters as seen in Fig. 18a, b. The accurate-shape siloes exhibit a lower impulsive load when compared to the rectangular geometry, relating directly to the dissipation of shock wave energy when interacting

with the intricate details of the higher fidelity silo models as opposed to a smooth surface. The rectangular geometry also exhibits arrivals of progressive waves at the measurement point resulting in spikes in the pressure history which the accurate geometry does not exhibit. It is believed that complexity of the initial interaction with the accurate geometry results in a greater amount of wave scattering and thus a reduction in the loading profile felt downstream of the obstacle when compared to the rectangular obstacle propagation scenario.

To quantify these differences across the full field of the event, the same biharmonic interpolation methodology was undertaken for the geometrically accurate results and normalised by the results from the rectangular silo data as seen in Fig. 19. On close inspection, pressure traces measured behind the accurate siloes model exhibit notable features. This could indicate more turbulent flow conditions behind the siloes due to the blast wave interacting with the series of semi-circular geometries as the waves diffract around the outer perimeter of the siloes obstacle.

While arrival time exhibits almost identical behaviour regardless of obstacle fidelity throughout the whole domain considered, the other loading parameters present localised

Fig. 19 Normalised heatmaps showing the interpolated results from the rectangular silo experiments normalised by the accurate silo results, showing the changes in spatial distribution of positive phase blast wave parameters with respect to obstacle fidelity





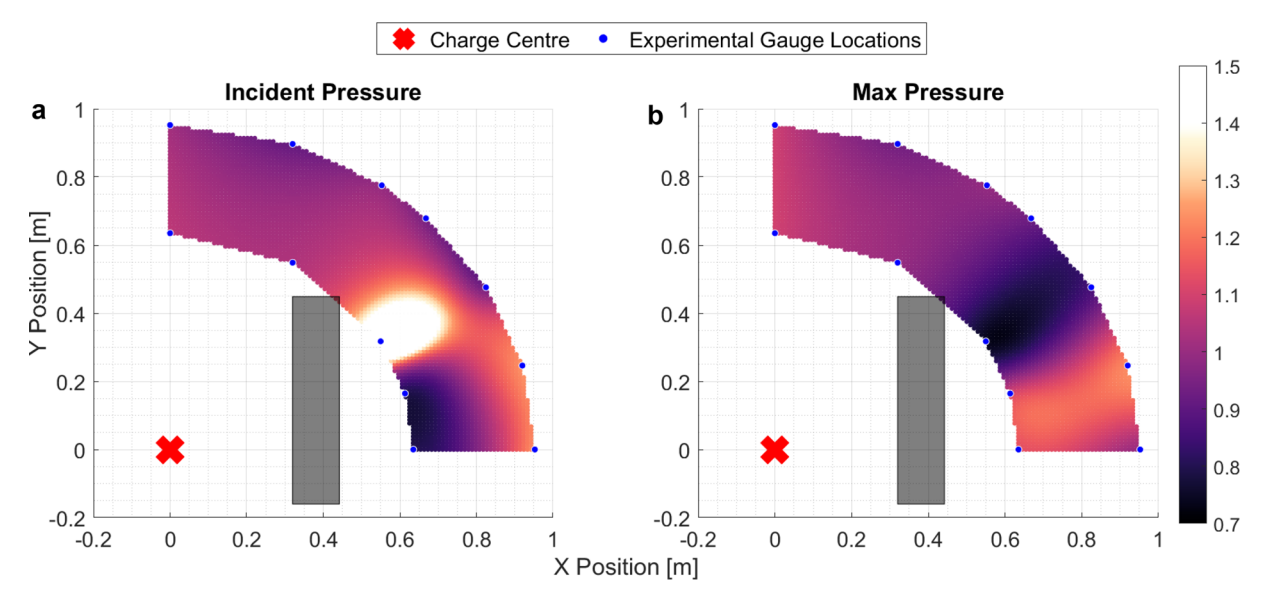


Fig. 20 Normalised heatmaps showing the interpolated results from the rectangular silo experiments normalised by the accurate silo results and demonstrating the changes in spatial distribution of **a** incident and **b** maximum overpressure with respect to obstacle fidelity

behavioural differences. It is important to consider the intense changes in peak measured pressure in the shielded region behind the obstacle. Here, up to a 40% increase is recorded between the geometrically accurate and rectangular building, believed to be related to variations in subtle changes in the arrival and hence superposition of the waves which have diffracted around the obstacle itself, creating localised spikes in different locations and times. Irrespective of these changes, impulsive loading is consistent throughout the domain when comparing the two obstacle fidelities, suggesting that for a full holistic understanding of blast loading downstream of an obstacle, fidelity is irrelevant.

Figure 20 presents variations of localised loading at different times that were dictated by obstacle fidelity. The first instance of blast wave arrival (i.e., incident pressure) in Fig. 20a shows both significant amplifications and reductions in pressure measurements when comparing the accurate to rectangular geometries. This is directly linked to the delayed arrival of incident shocks as a result of an increased amount of wave scattering when the accurate geometry is in position. The greater maximum pressure recorded in Fig. 20b is further evidence of this change in arrival times of the individual shocks and therefore the position of coalescence changing with obstacle fidelity. This finding in conjunction with a conserved specific impulse between the two geometries seen in Fig. 19 suggests that model fidelity is critical for understanding the location of coalescing waves and therefore is important for localised assessments of blast loading. This was evident for traces for gauge D2 (Fig. 21) as significant differences were observed between the two geometric fidelity scenarios, especially when compared to traces found for gauge D3 (Fig. 22).

3.2 Numerical results

CFD models identified four key blast-obstacle interaction processes (Fig. 23) that explain the local variations in pressure histories and loading at the locations surrounding the siloes obstacle observed in the experiments. Inspection of Fig. 23a, b shows the propagation of a reflected wave from the front face of the siloes obstacle, which explains the second pressure peak and increased specific impulse measured experimentally at gauge Y3. It can be observed that diffraction of blast waves around the silo obstacle laterally (Fig. 23b) and vertically (Fig. 23c) results in superposition behind the siloes, resulting in double pressure peaks and localised regions of higher overpressure within the shielded zone. Continued interference of the diffracted waves behind the siloes is responsible for further localised pressure increases and the return to a more uniform blast wavefront (Fig. 23d).

Pressure—time traces calculated by the numerical models are overlaid with experimental data for both the rectangular (Fig. 24) and accurate (Fig. 25) siloes obstacle tests, demonstrating excellent agreement of waveforms at all gauge locations.

The data presented in Fig. 26 are a comparison between the extracted mean experimental blast parameters to those from the CFD simulations with marker size representing grid cell size and colour (red or blue) denoting obstacle fidelity.

Blast wave parameters calculated by numerical models generally demonstrated limited sensitivity to the cell sizes explored in this study. However, some variations were observed for peak overpressure using different cell sizes at some gauge locations. This variation is present for two



Fig. 21 Compiled pressure histories from a 26.7-g PE4 hemispherical charge at gauge D2 ($Z = 2 \text{ m/kg}^{1/3}$) for both the rectangular and accurate geometry siloes: a overpressure and **b** specific impulse

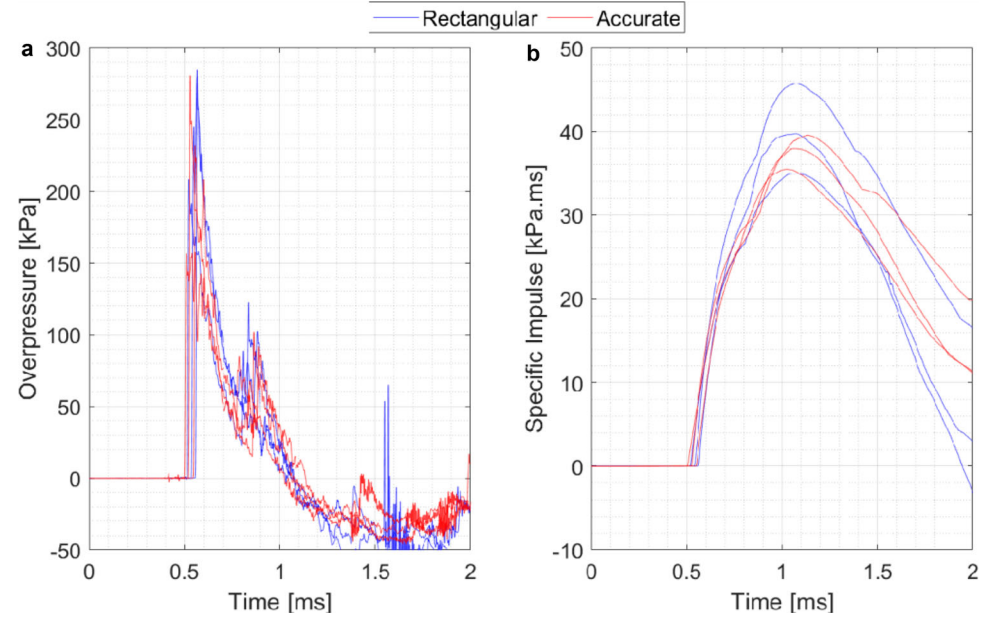
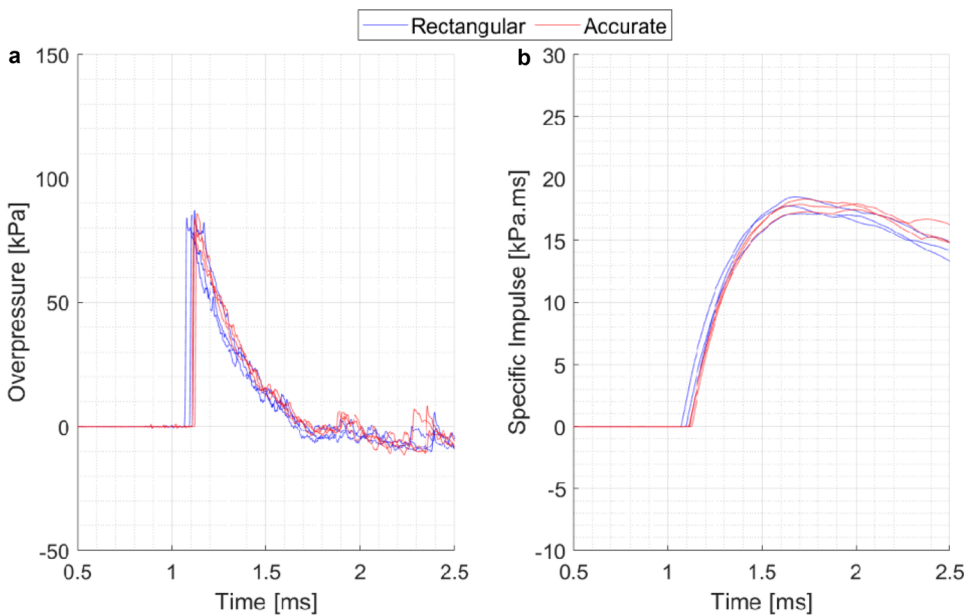


Fig. 22 Compiled pressure histories from a 26.7-g PE4 hemispherical charge at gauge D3 ($Z=3 \text{ m/kg}^{1/3}$) for both the rectangular and accurate geometry siloes: **a** overpressure and **b** specific impulse



opposing reasons. As cell size decreases, this increases the sharpness of the pressure spike(s), potentially leading to overprediction of pressure. However, as the cell size increases, and pressure peaks lose their distinctive features, individual coalescing waves begin to appear as a single pressure rise rather than two distinct peaks, which affects the incident and maximum overpressure readings. As such, in this scenario, it is not clear which cell size should be selected for overpressure specifically.

Blast wave arrival at each position was consistently ~ 10% early in the numerical simulations, although the other blast parameters presented more variability through this direct comparison. Despite generally over-predicting pos-

itive phase durations and specific impulses, the numerical models demonstrated relatively good agreement with experimental values, with the majority of gauge locations falling within the +10% boundaries (Fig. 26).

Agreement between the modelled and recorded peak overpressures was more variable and comparably lower than for other parameters, within the $\pm 20\%$ boundaries (Fig. 26). Extracted blast parameters were obtained through automated techniques without proven curve fitting approaches. In doing so, experimental electrical errors, associated with piezoelectric pressure gauges, have not been omitted in this comparison, thus resulting in more variable results for peak overpressure. Discrepancies between the results may also



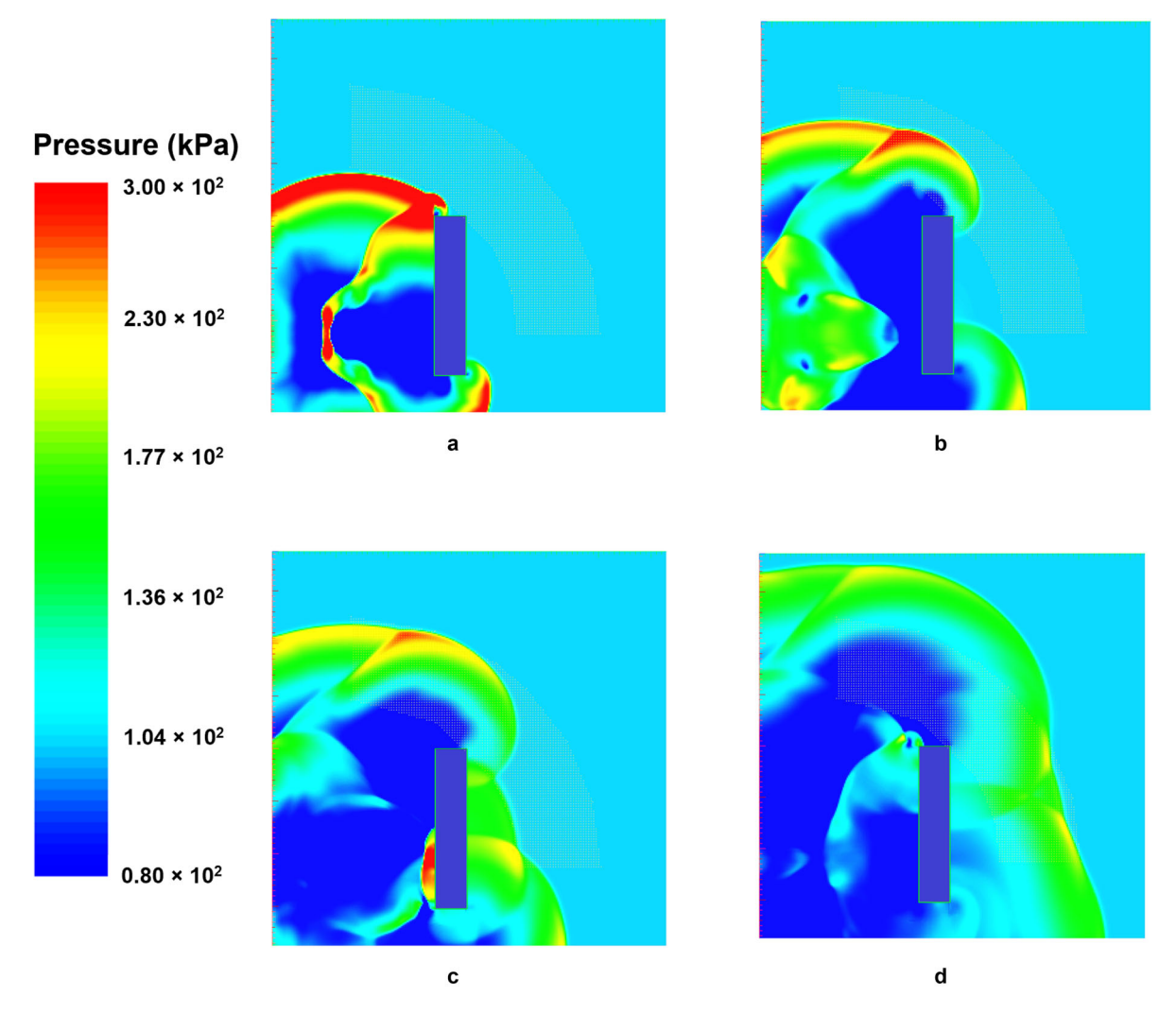


Fig. 23 CFD pressure contours showing the plan view evolution of blast wave interaction with the rectangular silo obstacles (5 mm cells) resulting in local loading variations. **a** t = 0.45 ms: Blast wave reflection off siloes' side/front elevation, causing elevated pressures at Y- and B-gauges. **b** t = 0.80 ms: Lateral blast wave diffraction

around obstacle into shielded zone, affecting gauges behind the siloes. $\mathbf{c}\ t=1.00\ \mathrm{ms}$: Vertical blast wave diffraction over the top of siloes obstacle into the shielded zone, affecting gauges behind the siloes. $\mathbf{d}\ t=1.50\ \mathrm{ms}$: Constructive interference of diffracted blast waves resulting in localised pressure increases behind the siloes

have been introduced by using a TNT material in the CFD models rather than PE4, as used in the experiments. Considering that all pressure gauges were located within relatively near-field blast conditions (i.e., $Z < 3 \, \text{m/kg}^{1/3}$), and therefore higher variability zone (as previously shown), achieving agreement within 20% was deemed acceptable.

Using a heatmap format, Fig. 27 presents extracted blast wave parameters from the numerical models for the accurate (column 1) and rectangular siloes (column 2) normalised by the KB predictions for the equivalent free-field case (siloes omitted), allowing inspection of the net effects of the siloes in comparison with the free-field case. Consistent with experimental findings, numerical models show that the presence of the siloes caused increased overpressure and impulse in

front of the siloes (due to reflection from the front wall) with decreased pressure and later arrival times occurring behind the siloes due to diffraction and shielding.

Comparing the heatmaps between columns 1 and 2 in Fig. 27, at a global scale, it appears that the geometry fidelity of the siloes obstacle has negligible effect on the distribution and magnitudes of the surrounding blast loading conditions. This is also visible in the pressure contours plot in Fig. 28, demonstrating very similar pressure magnitudes and distributions surrounding the siloes for both the rectangular and accurate obstacle, with positions of diffracted blast waves and superposition of wavefronts appearing largely similar in both cases at the same time point (t = 1.0 ms). This further confirms the experimental findings that obstacle fidelity



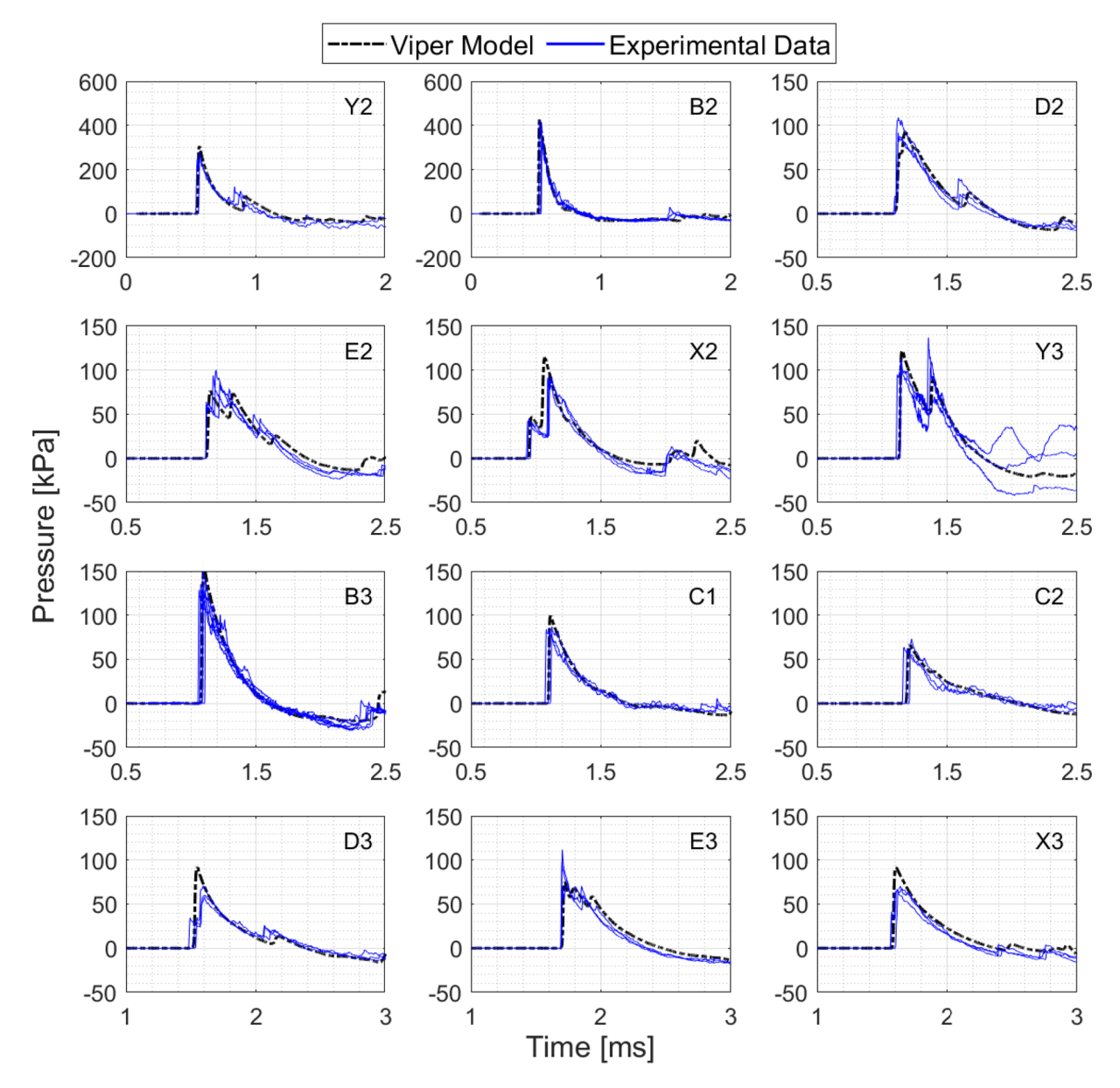


Fig. 24 Experimental results for the rectangular siloes geometry compared directly to CFD model results using 2 mm mesh size, which have been time shifted to align with experimental results (the amount of time shift for each plot varied slightly)

has relatively limited influence on surrounding blast wave loading conditions.

To inspect any differences between the two obstacle fidelities more closely, column 3 of Fig. 27 presents the net difference between the normalised accurate and rectangular modelling scenarios. At a global scale, numerical modelling results in column 3 of Fig. 27 show very little difference in the surrounding loading conditions (overpressure, specific impulse, and arrival times) between the rectangular and accurate siloes obstacles. Similar to the experimental findings, arrival times were consistent between both cases, with very slight variations in specific impulse (< 4%) in localised regions behind the siloes (Fig. 27).

As seen in Fig. 27, column 3, there were pressure differences of approximately 5% between the modelling results for the accurate and rectangular siloes, most noticeably in localised regions behind the siloes. Two reasons are proposed to explain the cause of these small differences.

Firstly, from inspection of the pressure contours in Fig. 28, it can be seen that the different silo geometries slightly affect the spatial location of coalescing wavefronts that have diffracted around the obstacle. This allows localised pressure hotspots (due to constructive interference) to occur in slightly different locations behind the siloes, which is responsible for the small net pressure differences when comparing between the two obstacle cases at fixed locations



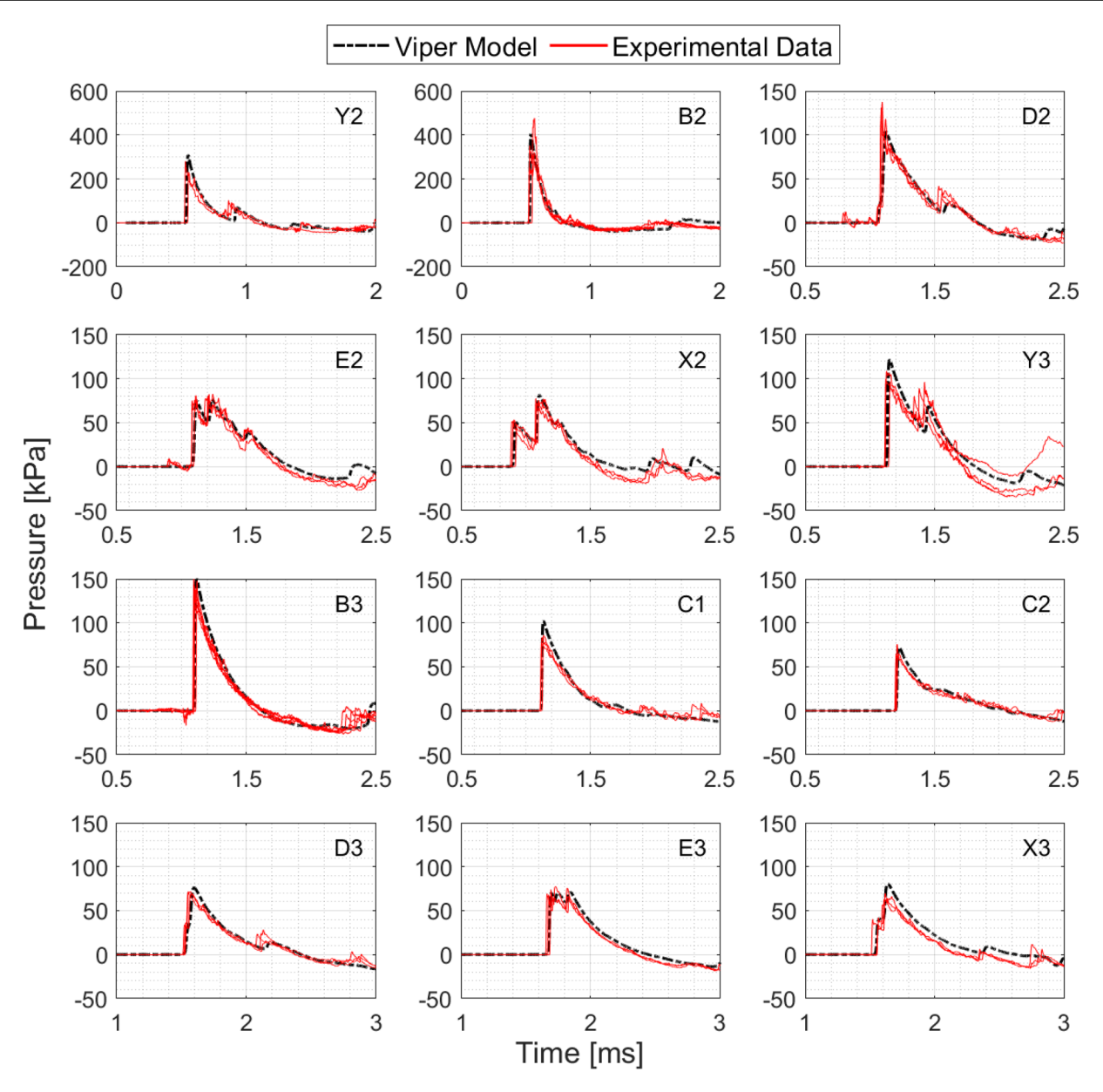


Fig. 25 Overlaid experimental results for the accurate siloes obstacle compared with CFD model results using 2 mm mesh size, which have been time shifted to align with experimental traces (the amount of time shift for each plot varied slightly)

(Fig. 27). As an example, the positioning of wavefront coalescence in the rectangular scenario is responsible for the higher maximum overpressure observed at X2 (Fig. 28), causing a relatively higher second peak in pressure (Fig. 25), which aligns with the experimental findings in Fig. 20b. Similarly, coalescence of wavefronts behind the rectangular siloes is responsible for the higher incident overpressure at D2, which aligns with the experimental findings in Fig. 20a.

Secondly, it can be seen in Fig. 28 that pressures are slightly lower in the reflective zone at B3 for the accurate siloes modelling results, which also aligns with the experimental findings. As the wavefront positioning is similar here,

it suggests that blast interaction with the cylindrical surface of the accurate siloes obstacle results in blast wave scattering, leading to slightly reduced peak overpressure and impulse in comparison with the rectangular siloes case, which features a uniform reflecting surface.

Other than the localised and minor discrepancies in peak overpressure, numerical models confirm that the obstacle fidelity had limited impact on the blast loading effects experienced around the obstacle.



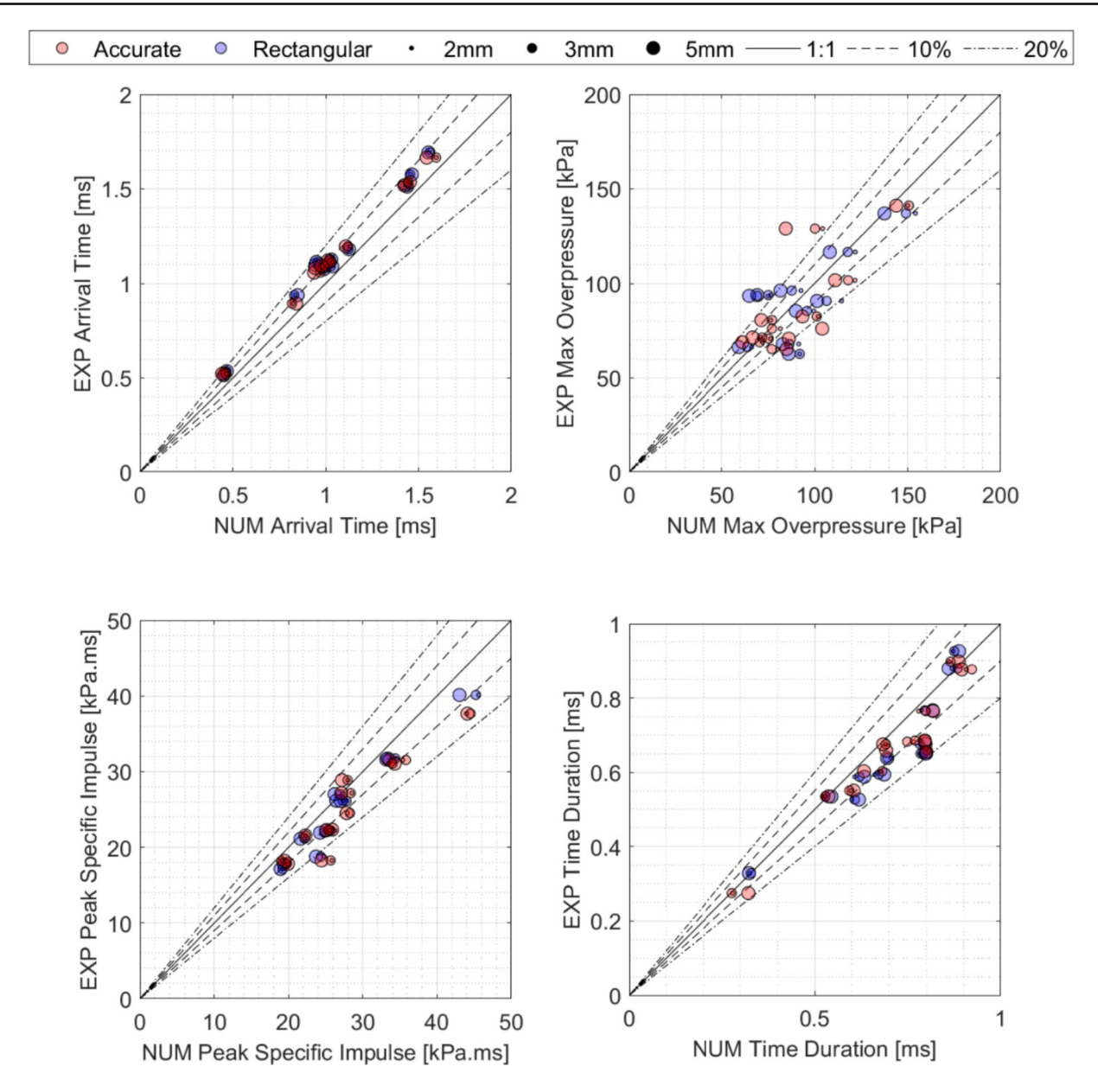


Fig. 26 The comparison of positive phase blast wave parameters calculated by CFD models with mean experimental results

3.2.1 Evaluating downstream shielding effects

Numerical models with the extended domain show that the shielding effect from the siloes (i.e., net reduction in overpressure) decreases with increasing blast scaled distance. Shielded pressures become similar to incident blast conditions by $Z=5\,\mathrm{m/kg^{1/3}}$ (Fig. 29), equivalent to 397 m at full scale, which is slightly less than the 450 m distance proposed by Zehil [8]. As discussed previously, there are some initial differences in maximum overpressure between the two geometric representations of the siloes for 2 m/kg^{1/3} < Z < 3 m/kg^{1/3}; however, peak pressures are seen to effectively converge beyond $Z=4\,\mathrm{m/kg^{1/3}}$. This confirms that

any minor differences in overpressure related to differing obstacle fidelities can be expected to cease in the far field.

As seen in Fig. 29, the specific impulse behind the siloes is initially lower than the free-field case but then exceeds the free-field scenario for distances beyond $Z=4.5 \text{ m/kg}^{1/3}$. This is due to the superposition of diffracted blast waves behind the siloes causing a waveform with multiple peaks and extended time duration, resulting in relatively higher specific impulses further afield.

While shielded overpressures appear to converge to the free-field case (without siloes) by approximately $Z = 5 \text{ m/kg}^{1/3}$, it is important to note that a small reduction in pressure still persists behind the siloes into the far field. For



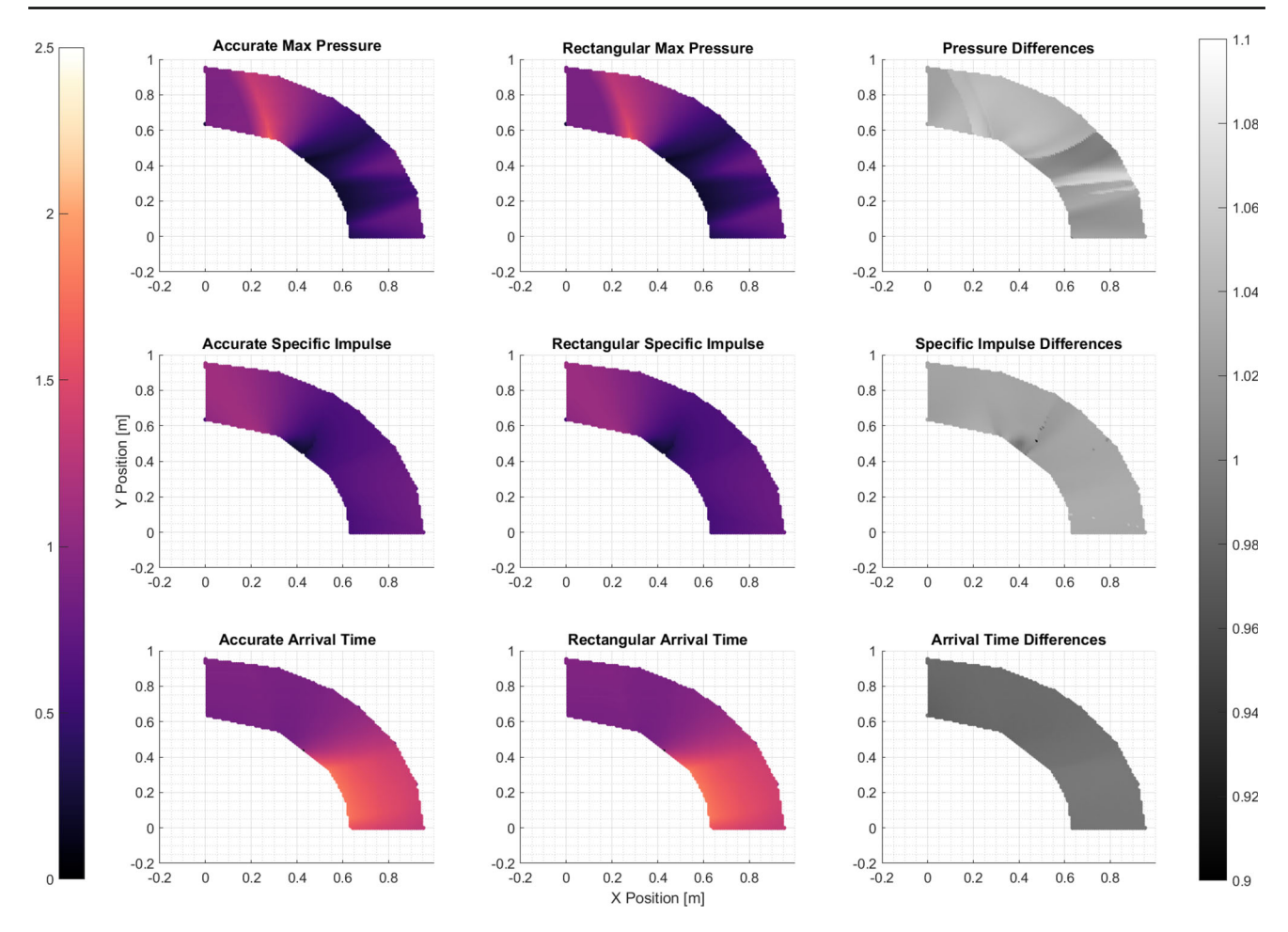


Fig. 27 Rectangular (column 1) and accurate (column 2) numerical modelling results normalised by the Kingery–Bulmash predictions for the equivalent free-field case (siloes omitted) and net difference (column 3)

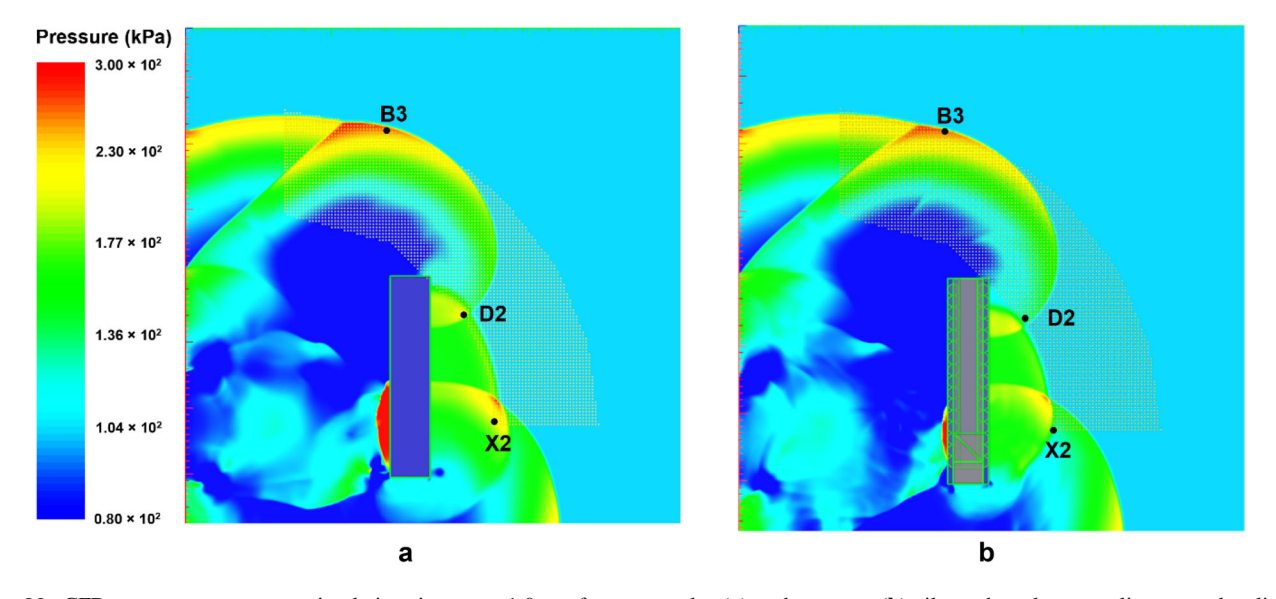


Fig. 28 CFD pressure contours at simulation time t = 1.0 ms for rectangular (a) and accurate (b) siloes obstacles, revealing some localised discrepancies in peak overpressures



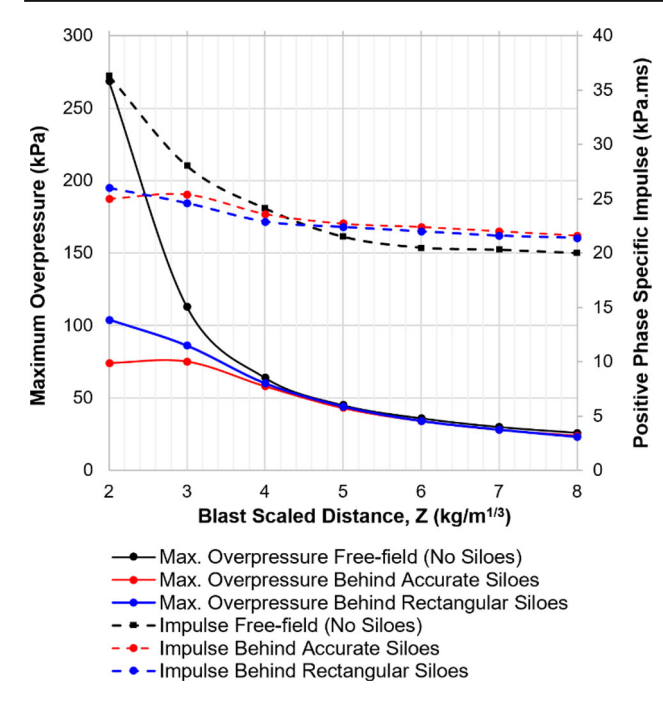
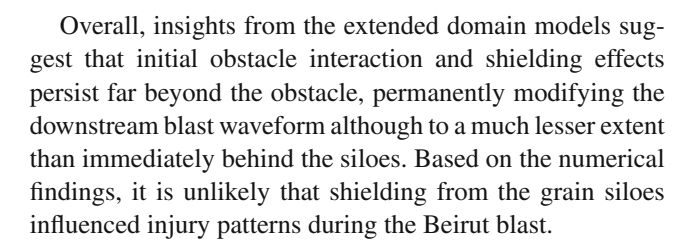


Fig. 29 Numerical results from the extended domain models examining maximum overpressure and specific impulse with increasing blast scaled distance for the free field and both siloes scenarios

example, at $Z = 8 \text{ m/kg}^{1/3}$, corresponding to 635 m at full scale (where residential areas begin surrounding the port), models for the accurate silos predict a 2-kPa pressure reduction (-7.7%) compared to the free-field scenario (without the siloes). At these distances, predicted peak overpressures were $p_i = 25$ kPa, below the lowest pressure threshold for "primary" blast injuries [47] (i.e., 35 kPa for threshold risk of tympanic membrane (ear drum) rupture). As a result, it is unlikely that these minor reductions in overpressure behind the siloes in the far field ($Z > 8 \text{ m/kg}^{1/3}$) will have directly influenced primary blast injury risk. However, such a pressure reduction may have non-trivial consequences for glazing failure, which is prone to failure in the low overpressure, long duration loading regime [48]. This is particularly important given that the majority of those injured by the Beirut blast suffered lacerations, predominantly caused by broken windows [49, 50].

Although counter-intuitive, numerical models also predicted increased specific impulse behind the siloes in the far field compared to the free-field scenario. At the experimental scale (1:250), models predicted a modest impulse increase behind the accurate siloes (\sim 1.6 kPa ms at $Z=8\,\text{m/kg}^{1/3}$); however, based on the principles of Hopkinson-Cranz scaling [22, 23], this amplification would be much larger at full scale (\sim 400 kPa ms). Importantly, increased impulse is associated with increased structural damage [51] and blast injury risk [52].



4 Limitations and further work

A key limitation of this study is the representation of the siloes as a perfectly rigid obstacle. As was apparent in the immediate aftermath of the disaster [3], multiple siloes were destroyed during the explosion. The extent to which this structural damage influenced blast propagation around the siloes is unknown, although it is expected that energy was absorbed through the deformation of the damaged siloes and, depending on the timing/transient response of the siloes structures relative to the blast wave, volumetric material loss of the obstacle may also have contributed to modified blast propagation behaviour.

While so-called fluid–structure interaction effects have been well explored for homogenous/predominantly metallic deformable structures [53, 54], significantly less is understood about the effect of frangible structures, particularly where obstacles undergo large volumetric losses due to blast damage. Such effects are complex to investigate experimentally, and no predictive methods currently account for such behaviour. Given the increasing reliance on CFD for city-scale blast analyses assuming fully rigid structures, it remains important to improve understanding of how structural damage and obstacle frangibility affects blast propagation behaviour and loading effects. Further work should investigate the effects of blast wave interaction with frangible obstacles to determine how structural damage influences blast propagation behaviour.

Other inaccuracies were also introduced by some geometry simplifications and assumptions underpinning the experimental setup, including the assumed equivalent explosive mass and idealised charge shape. The geometry of the accurate siloes obstacle tested in this study was informed by dimensions reported in literature; however, some features will have been neglected, thus simplifying the true grain siloes geometry. In these tests, the effects of the terrain surrounding the siloes were neglected; it was assumed to be perfectly flat. While this is an acceptable representation of the nearby surroundings of the port, changes in elevation further afield will have slightly influenced far-field loading effects [28, 55].

The experimental setup and numerical models simplified the environment surrounding the grain siloes by omitting warehouses and other structures. Although these structures



were completely destroyed by the explosion, they may have locally influenced blast wave propagation behaviour, although such effects are expected to have had relatively limited influence in this case. More broadly, little is understood about the extent that relatively smaller sub-structures influence blast wave propagation around the primary structural obstacle. This knowledge gap is highly relevant to urban blast modellers facing decisions about which obstacles (e.g., street furniture and minor structural forms) are significant and necessitate inclusion in such analyses.

In this study, blast propagation and shielding effects were tested experimentally over a relatively limited, near-field ($Z < 3 \text{ m/kg}^{1/3}$) region. While verified numerical models provided insights into the far-field ($Z = 8 \text{ m/kg}^{1/3}$) obstacle shielding behaviour, further experiments should be undertaken to verify these observations.

5 Conclusions

Findings from this study confirmed that the Beirut grain siloes caused shielding, characterised by locally reduced overpressures, specific impulses and increased blast wave arrival times in the shielded zone behind the structure. While numerical models indicated that shielded pressures effectively ceased by $Z=5\,\mathrm{m/kg^{1/3}}$, counter-intuitively, specific impulses were slightly amplified behind the silos in the far field. However, due to modest differences between the incident and shielded loading conditions in the far field, it was deemed unlikely that the siloes influenced structural damage or injury risk in Beirut's western region surrounding the port.

Blast wave parameters surrounding the siloes did not exhibit significant differences between the cuboid and accurate representation of the siloes geometry, suggesting that obstacle fidelity has negligible influence on blast propagation and surrounding loading conditions. Some minor differences (10%) in peak overpressure were identified in localised regions, attributed to the two differing fidelities. Insights from numerical models explained that these were caused by modified blast wave diffraction and superposition behaviour. This was responsible for altering the location of constructive interference and the spatial distribution of peak overpressures in the shielded zone. The repeating cylindrical surface profile of the accurate siloes also resulted in greater blast wave scattering, which modestly reduced peak overpressure in the reflective zone. As the observed overpressure discrepancies were small and very localised, it was deemed that such differences would only become important for very specific cases (e.g., insurance or demolishing services may find it particularly useful). In the context of undertaking urban blast loading assessments, the findings suggest that neglecting architectural details and simplifying the gross outer geometry of structural obstacles provides acceptable accuracy.

CFD models demonstrated excellent agreement with experimental results, showing the capability to replicate the minor pressure differences associated with each obstacle geometry. This underscores the role of CFD as a reliable tool for undertaking more complex blast-obstacle interaction scenarios at different geometric fidelities, as part of larger urban blast analyses. Some sensitivity was observed between modelling cell size and predicted peak overpressures, highlighting the importance of understanding the effects and potential limitations associated with selecting different cell sizes for modelling blast-obstacle interaction phenomena. Despite these differences, when considering the context of emergency decision-making in response to an urban blast event, this case study has demonstrated that reasonable accuracy can be achieved by assuming simplified cuboidal obstacles and by using a relatively coarse (5 mm cell size) CFD model, enabling results in a relatively fast time frame (i.e., sub-20 min run time).

Acknowledgements The research leading to these results received funding from the Worldwide Universities Network (WUN) Research Development Fund (RDF) 2022 round.

Data Availability The data supporting the findings of this study are not available online due to the large volume and size of the files. Data sets generated during the current study are available from the corresponding author on reasonable request.

Declarations

Conflict of interest The authors have no conflict of interest to declare that are relevant to the content of this article.

Open Access This article is licensed under a Creative Commons Attribution 4.0 International License, which permits use, sharing, adaptation, distribution and reproduction in any medium or format, as long as you give appropriate credit to the original author(s) and the source, provide a link to the Creative Commons licence, and indicate if changes were made. The images or other third party material in this article are included in the article's Creative Commons licence, unless indicated otherwise in a credit line to the material. If material is not included in the article's Creative Commons licence and your intended use is not permitted by statutory regulation or exceeds the permitted use, you will need to obtain permission directly from the copyright holder. To view a copy of this licence, visit https://creativecommons.org/licenses/by/4.0/.

References

- Sawaya, G.: Beirut's grain silos: the monolith that shielded the city during 2020's port blast. https://www.designboom.com/ architecture/beiruts-grain-silos-the-monolith-that-shielded-thecity-02-04-2021/. Accessed 17 August 2023
- Landry, M.D., Alameddine, M., Jesus, T.S., Sassine, S., Koueik, E., Raman, S.R.: The 2020 blast in the Port of Beirut: can the Lebanese health system "build back better"? BMC Health Serv. Res. 20(1), 1040 (2020). https://doi.org/10.1186/s12913-020-05906-y



- Temsah, Y., Jahami, A., Aouad, C.: Silos structural response to blast loading. Eng. Struct. 243, 112671 (2021). https://doi.org/10. 1016/j.engstruct.2021.112671
- Ismail, S., Raphael, W., Durand, E.: Monitoring the Beirut Port Silos' structural health response a few months after blast loading using 3D laser scan. Jordan J. Civil Eng. 15, 489–505 (2021). https://jjce.just.edu.jo/Home/ShowPaper.aspx? data=OR1Svb52LP92MqfKmILmPK8ziMvdTXqLavK4ZUQlzdw %3d
- News Wires: More grain silos collapse at Beirut port, damaged by devastating 2020 blast. FRANCE 24 (2022). https://www.france24.com/en/middle-east/20220823-more-grain-silos-collapse-at-beirut-port-damaged-by-devastating-2020-blast
- Ismail, S., Raphael, W., Durand, E.: Case study of the Beirut port explosion using 3D laser scan and nonlinear finite element model. Res. Eng. Struct. Mater. 7(4), 551–577 (2021). https://doi.org/10. 17515/resm2021.286st0428
- Sadek, S., Dabaghi, M., O'donnell, T.M., Zimmaro, P., Hashash, Y., Stewart, J.P.: Impacts of 2020 Beirut Explosion on Port Infrastructure and Nearby Buildings. Nat. Hazard. Rev. 23(2), 04022008 (2022). https://doi.org/10.1061/(ASCE)NH.1527-6996.0000550
- Zéhil, G.P.: Investigating the Blast Shielding Effect of the Beirut Silos. Shock Waves 34(3), 227–235 (2024). https://doi.org/10. 1007/s00193-024-01189-y
- Morsel, A., Masi, F., Marché, E., Racineux, G., Kotronis, P., Stefanou, I.: MiniBLAST: a Novel Experimental Setup for Laboratory Testing of Structures Under Blast Loads. Exp. Tech. 49, 655–675 (2025). https://doi.org/10.1007/s40799-024-00771-4
- Gajewski, T., Sielicki, P.W.: Experimental Study of Blast Loading Behind a Building Corner. Shock Waves 30(4), 385–394 (2020). https://doi.org/10.1007/s00193-020-00936-1
- Gautier, A., Sochet, I., Lapebie, E.: Analysis of 3D Interaction of a Blast Wave with a Finite Wall. Shock Waves 32(3), 273–282 (2022). https://doi.org/10.1007/s00193-022-01081-7
- Gautier, A., Sochet, I., Lapebie, E., Boubrit, A.: Shock Wave Propagation in an Obstructed Area. Wit. Trans. Built. Environ. 198, 15–27 (2020). https://doi.org/10.2495/SUSI200021
- Dela Cueva, J., Zheng, L., Lawlor, B., Nguyen, K., Westra, A., Nunez, J., Zanteson, J., Mcguire, C., Chavez Morales, R., Katko, B.J., Liu, H., Eliasson, V.: Blast Wave Interaction with Structures: an Application of Exploding Wire Experiments. Multisc. Multidiscip. Model. Exp. Design 3(4), 337–347 (2020). https://doi.org/10. 1007/s41939-020-00076-0
- Farrimond, D., Ratcliff, A., Dennis, A., Rigby, S., Tyas, A., Clarke, S., Lodge, T., Tolman, W.: MicroBlast - a benchmarking study of gramme-scale explosive trials. 26th International Symposium on Military Aspects of Blast and Shock (MABS26), Wollongong, Australia (2023). https://eprints.whiterose.ac.uk/206198/
- Hopkinson, B.: British Ordnance Board Minutes 13565, The National Archives, Kew, UK, vol. 11 (1915)
- 16. Cranz, K. J., Lehrbuch der ballistik. Рипол Классик (1925)
- Gabriel, S., Denny, J., Chung Kim Yuen, S., Langdon, G.S., Govender, R.A.: The effect of scaling building configuration blast experiments on positive phase blast wave parameters. Appl. Sci. 13(10), 5956 (2023). https://doi.org/10.3390/app13105956
- Needham, C. E.: Blast loads and propagation around and over a building. In: Hannemann, K., Seiler, F. (eds.) Shock Waves. 26th International Symposium on Shock Waves, Vol. 2, pp. 1359–2364. Springer, Berlin, Heidelberg. https://doi.org/10.1007/978-3-540-85181-3 91
- Löhner, R., Baum, J. D., Rice, D.: Comparison of coarse and fine mesh 3-D Euler predictions for blast loads on generic building configurations. 18th International Symposium on Military Aspects of Blast and Shock (MABS18), Bad Reichenhall, Germany (2004)

- Dib, N., Zéhil, G.-P., Rigby, S.: On the Blast-wave Shielding Effect of Porous Buildings. J. Fluids Struct. 115, 103787 (2022). https:// doi.org/10.1016/j.jfluidstructs.2022.103787
- Marks, N.A., Stewart, M.G., Netherton, M.D., Stirling, C.G.: Airblast Variability and Fatality Risks from a VBIED in a Complex Urban Environment. Reliab. Eng. Syst. Saf. 209, 107459 (2021). https://doi.org/10.1016/j.ress.2021.107459
- Remennikov, A.M., Rose, T.A.: Modelling Blast Loads on Buildings in Complex City Geometries. Comput. Struct. 83(27), 2197–2205 (2005). https://doi.org/10.1016/j.compstruc.2005.04.003
- Luccioni, B., Ambrosini, D., Danesi, R.: Blast Load Assessment Using Hydrocodes. Eng. Struct. 28(12), 1736–1744 (2006). https://doi.org/10.1016/j.engstruct.2006.02.016
- Valsamos, G., Larcher, M., Casadei, F.: Beirut Explosion 2020: a Case Study for a Large-scale Urban Blast Simulation. Saf. Sci. 137, 105190 (2021). https://doi.org/10.1016/j.ssci.2021.105190
- Yandex. Beirut. DigitalGlobe, Inc. https://yandex.com/maps/ 11497/beirut/satellite/?from=api-maps&ll=35.518594%2C33.
 901120&origin=jsapi_2_1_79&z=17. Accessed 12 August 2023
- Bogosian, D., Yokota, M., Rigby, S. E.: TNT equivalence of C-4 and PE4: a review of traditional sources and recent data. 24th International Symposium on Military Aspects of Blast and Shock (MABS24), Halifax, Canada (2016). https://eprints.whiterose.ac. uk/105008/
- Sielicki, P., Rigby, S.: An Investigation of TNT Equivalence of Hemispherical PE4 Charges. Eng. Trans. 62, 423–435 (2014). https://doi.org/10.24423/engtrans.266.2014
- Leconte, R., Terrana, S., Giraldi, L.: Predicting Terrain Effects on Blast Waves: an Artificial Neural Network Approach. Shock Waves 35, 37–55 (2024). https://doi.org/10.1007/s00193-024-01206-0
- Forensic Architecture. The Beirut Port explosion: destruction of destruction. https://forensic-architecture.org/investigation/thebeirut-port-explosion-destruction-of-destruction. Accessed 21 August 2024
- 30. Rigby, S., Isaac, O., Alshammari, O., Clarke, S.: Can fractals mitigate blast loading? In: Earthquake Engineering and Dynamics for a Sustainable Future, 2023 Society for Earthquake and Civil Engineering Dynamics (SECED) Conference, 14-15 September, Cambridge, UK (2023). https://www.seced.org.uk/index.php/seced-2023-proceedings/62-blast-impact-and-vibration/783-can-fractals-mitigate-blast-loading
- PCB Piezotronics. Dynamic Pressure Sensors for High Frequency Measurements (2024). Available: https://www.pcb.com/contentstore/mktgcontent/linkeddocuments/pressure/TM-PRS-113B-102B_lowres.pdf
- 32. Stirling, C. (ed.): Viper::Blast. Stirling Simulation Services Limited, Edinburgh, Scotland (2021)
- Rose, T. A.: An approach to the evaluation of blast loads on finite and semi-infinite structures. PhD Thesis, Engineering Systems Department, Cranfield University (2010). https://dspace.lib. cranfield.ac.uk/items/a5dee66c-1a9f-4459-b18d-1be5caccac88
- Wada, Y., Liou, M.-S.: An Accurate and Robust Flux Splitting Scheme for Shock and Contact Discontinuities. SIAM J. Sci. Comput. 18(3), 633–657 (1997). https://doi.org/10.1137/S1064827595287626
- Farrimond, D.G., Woolford, S., Tyas, A., Rigby, S.E., Clarke, S.D., Barr, A., Whittaker, M., Pope, D.J.: Far-field Positive Phase Blast Parameter Characterisation of RDX and PETN Based Explosives. Int. J. Protect. Struct. 15(1), 141–165 (2024). https://doi.org/10. 1177/20414196221149752
- Shin, J., Whittaker, A.S., Cormie, D.: TNT Equivalency for Overpressure and Impulse for Detonations of Spherical Charges of High Explosives. Int. J. Protect. Struct. 6(3), 567–579 (2015). https://doi.org/10.1260/2041-4196.6.3.567
- Whittaker, M., Klomfass, A., Softley, I., Pope, D., Tyas, A.: Comparison of numerical analysis with output from precision diag-



- nostics during near-field blast evaluation. Proceedings of 18th International Symposium on Interaction of the Effects of Munitions with Structures (ISIEMS18), pp. 21–25 (2019)
- 38. Dobratz, B.M., Crawford, P.C.: LLNL Explosives Handbook, Properties of Chemical Explosives and Simulants. Livermore National Laboratory, Livermore, CA (1985)
- Lee, E., Hornig, H., Kury, J.: Adiabatic Expansion of High Explosive Detonation Products. Univ. of California Radiation Lab, Livermore, Livermore, CA (1968)
- Tyas, A.: Blast loading from high explosive detonation: what we know and what we don't know. Proceedings of 13th International Conference on Shock and Impact Loads on Structures, Guangzhou, China, pp. 65–67 (2019)
- Rigby, S.E., Knighton, R., Clarke, S.D., Tyas, A.: Reflected Nearfield Blast Pressure Measurements Using High Speed Video. Exp. Mech. 60(7), 875–888 (2020). https://doi.org/10.1007/s11340-020-00615-3
- Bogosian, D.D., Ferritto, J.M., Shi, Y.: Measuring uncertainty and conservatism in simplified blast models. 30th Explosives Safety Seminar, Atlanta (2002)
- Mendham, E., Rigby, S., Farrimond, D., Tyas, A., Pezzola, G.: Far field blast parameters from cuboidal charges. Proceedings of the 4th International Conference on Structural Safety Under Fire & Blast Loading (CONFAB 2024), ASRANet Ltd., London (2024)
- Sherkar, P., Shin, J., Whittaker, A., Aref, A.: Influence of Charge Shape and Point of Detonation on Blast-resistant Design. J. Struct. Eng. 142(2), 04015109 (2016). https://doi.org/10.1061/ (ASCE)ST.1943-541X.0001371
- 45. Rose, T., Smith, P.: An approach to the problem of blast wave clearing on finite structures using empirical procedures based on numerical simulations. 16th International Symposium on Military Aspects of Blast and Shock (MABS16), Oxford, England (2000)
- Rose, T.A., Smith, P.D., Mays, G.C.: The Effectiveness of Walls Designed for the Protection of Structures Against Airblast from High Explosives. Proc. Inst. Civil Eng. Struct. Build. 110(1), 78– 85 (1995). https://doi.org/10.1680/istbu.1995.27306
- Denny, J., Dickinson, A., Langdon, G.: Guidelines to inform the generation of clinically relevant and realistic blast loading conditions for primary blast injury research. BMJ Mil Health 169(4), 364–369 (2023). https://doi.org/10.1136/bmjmilitary-2021-001796

- Glasstone, S., Philips, D.J.: The effects of nuclear weapons. U.S. Department of Defense and the Energy Research and Development Administration, Technical report (1977). https://www.govinfo.gov/content/pkg/GOVPUB-D-PURL-gpo106759/pdf/GOVPUB-D-PURL-gpo106759.pdf
- Denny, J., Batchelor, J., Al-Hajj, S.: Estimating blast exposures from the 2020 Beirut explosion and examining correlation with blast injuries. 26th International Symposium on Military Aspects of Blast and Shock (MABS26), Wollongong, Australia (2023)
- Glenny-Brown, R., Denny, J., Al-Hajj, S., Wild, H., Tacci, J., Onggo, S., Arruda, E., Von Bertele, M., Zaghloul, F., Batchelor, J.: Understanding Health Challenges, Response and Recovery: The 2020 Beirut Blast and Mass Casualty Blast Events. University of Southampton (2024). http://eprints.soton.ac.uk/id/eprint/486899
- Hardwick, M.J., Hall, J., Tatom, J.W., Baker, R.G.: Approved methods and algorithms for DoD risk-based explosives sitting. DDESB Technical Paper, PT Research Inc Huntsville Al., vol. 14 (2009). https://apps.dtic.mil/sti/pdfs/ADA507495.pdf
- Ferradás, E.G., Alonso, F.D., Miñarro, M.D., Aznar, A.M., Gimeno, J.R., Pérez, J.: Consequence Analysis by Means of Characteristic Curves to Determine the Damage to Humans from Bursting Spherical Vessels. Process Saf. Environ. Prot. 86(2), 121–129 (2008). https://doi.org/10.1016/j.psep.2007.10.004
- Aune, V., Valsamos, G., Casadei, F., Langseth, M., Børvik, T.: Fluid-structure Interaction Effects During the Dynamic Response of Clamped Thin Steel Plates Exposed to Blast Loading. Int. J. Mech. Sci. 195, 106263 (2021). https://doi.org/10.1016/j.ijmecsci. 2020.106263
- Børvik, T., Hanssen, A.G., Langseth, M., Olovsson, L.: Response of Structures to Planar Blast Loads—A Finite Element Engineering Approach. Comput. Struct. 87(9–10), 507–520 (2009). https://doi. org/10.1016/j.compstruc.2009.02.005
- Cannon, L., Rogers, A., Taggart, C.: Investigating the Significance of Non-ideal Effects in Large-scale Blast Propagation. Int. J. Protect. Struct. 16(1), 154–169 (2025). https://doi.org/10.1177/20414196241271449

Publisher's Note Springer Nature remains neutral with regard to jurisdictional claims in published maps and institutional affiliations.

